universität wien

MASTERARBEIT / MASTER'S THESIS

Titel der Masterarbeit / Title of the Master's Thesis

„Multilineage organoids as a model of neural crest lineage development and disease“

verfasst von / submitted by

Sophia Hannes, B.Sc.

angestrebter akademischer Grad / in partial fulfillment of the requirements for the degree of

Master of Science (MSc)

Wien, 2023 / Vienna, 2023

Studienkennzahl lt. Studienblatt / degree programme code as it appears on the student record sheet:	UA 066 877
Studienrichtung lt. Studienblatt / degree programme as it appears on the student record sheet:	Masterstudium Genetik und Entwicklungsbiologie
Betreut von / Supervisor:	Univ.Prof. Igor Adameyko, PhD

Table of Contents

List of Figures

List of Abbreviations

CHIR	CHIR 99021
CS	Carnegie stage
dsc	days in suspension culture
EMLO	elongating multi-lineage organized
GF	growth factors
hiPSC	human induced pluripotent stem cells
hpSC	human pluripotent stem cell
MIFF	ShiPS-miFF1
NCC	neural crest cells
PFA	paraformaldehyde
PNS	peripheral nervous system
SCP	schwann cell precursors
STAN	STAN062i-164-2

Acknowledgments

The Adameyko Lab is a lively one; A lab filled with brilliant scientists and truly outstanding personalities. Thank you, Igor, for welcoming me to this unique group of individuals, providing guidance, and sharing your hilarious tales at the kitchen table. My heartfelt thanks to Polina, who intuitively knew when to guide and when to let me soar independently—your kindness and support were invaluable.

Johan, our nerdy discussions about marble machines and bionic robot arms often left my head spinning. Rozalina, thank you for spicing up my life with gossip, your infectious laughter, and impromptu twerk sessions. My lab sis Miray, you have been a source of inspiration and joy ever since that first coffee at Pelikan. Marilena! Your advice and encouragement, both as a scientist and a friend, have been indispensable on this journey.

Beyond the sterile confines of the lab, my loved ones provided continuous joy and encouragement – Thank you for every precious second and unforgettable adventures. Omar, thank you for enduring endless rants about the “babies” (a.k.a. gastruloids). Maja, my soulgal, our (literal) tea sessions were a sanctuary in challenging times. Conni/Mausebein, you are my steady anchor through every storm. And finally, Laurin, thank you for keeping me sane. A special thank you goes to my mother and sister: Thank you for your unwavering support.

After all is said and done, three treasures will remain: The euphoria of scientific achievement, the warmth and love you bestowed upon me, and the quirky habit my phone developed, substituting “good” with “hood”. — I am profoundly grateful.

Abstract

Multipotent, migratory progenitors neural crest cells (NCC) and their multipotent derivatives, peripheral-nerve-associated Schwann cell precursors (SCP), contribute to a diverse spectrum of cell types, ranging from the cells of the peripheral nervous system to pigment-producing melanocytes. In addition to their vast developmental repertoire, these progenitors' malignant transformation has been implicated in a range of NCC-associated pathologies including paediatric cancer neuroblastoma. However, due to a lack of early human developmental models, characterization of human-specific aspects of NCCs and SCPs cell fate decisions remains challenging. Here I utilize the potential of three-dimensional (3D) in vitro organoids to generate a human-induced pluripotent stem-cell-based model of NCCs/SPCs lineage decisions. I demonstrate that gastruloids exposed to prolonged incubation with Wnt-agonist CHIR 99021, robustly display early developmental hallmarks such as early symmetry breaking, NCCs induction, and nerve-association of SCPs-like cells. Additionally, mature organoids express cell type-specific biomarkers of NCC/SCP derivatives autonomic neurons, and chromaffin cells. Finally, these data reinforce the importance of stringent assessment of iPSC lines' pluripotency states, as a guiding principle in organoid protocol optimization. Subsequently, this *in vitro* model provides a novel platform to investigate the molecular determinants that drive cell fate decisions, transitory states, and malignancies of NCC and SCPs in high spatiotemporal resolution.

Keywords: gastruloid, neural crest, neural crest lineage, fate reprogramming, peripheral nervous system, neuroblastoma

Introduction

Neural crest cells (NCC) are a neuroectoderm-derived population of multipotent, self-renewing, progenitor cells, often referred to as the 4th germ layer due to their vast developmental repertoire. As such, NCCs give rise to not only the ectomesenchymal cells of the face, and heart but also constitute the sensory- and autonomic nervous system, including enteric-, parasympathetic- and sympathetic neurons, peripheral glia, chromaffin cells and melanocytes[1,2]. NCCs are induced during gastrulation and become morphologically recognizable during neurulation at the neural plate border. Here closure of the neuroepithelium prompts epithelial-mesenchymal transition, delamination, and migration of NCCs[3,4]. During migration, NCCs undergo fate commitment biased by their initial spatiotemporal code[2,5,6] and environment [3,7].

While the exact mechanisms that govern NCC fate decisions and free migration are reviewed elsewhere[2,4,8–10], the main focus of this thesis is a subset of NCCs, that are tethered to outgrowing nerves and become Schwann cell precursors (SCPs). SCPs are multipotent, neural-crest-like cells, that use nerves for transportation and as stem cell niche[11]. As such NCCs and SCPs share a gene expression of marker- and downstream genes[1,11], as well as derivatives including melanocytes, chromaffin cells, autonomic neurons, and peripheral glia[1,11,12]. During their differentiation, NCCs/SCPs undergo a complex variety of transitional cell fates. One such state was characterized as a transcriptional multipotent “hub”/SCP state of biased NCC/SCP (*Itga4*, *Serpine2*, *Sox8*) preceding lineage commitment, in both murine NCC/SCP[6,13] and the developing human sympathoadrenal system[14].

In addition to their developmental importance, pathologies like melanoma[15,16], neurofibromatosis[17], and neuroblastoma[14,18–20] have been implicated as NCC/SCP-derived. For example, neuroblastoma, the most common extracranial solid paediatric tumor[19], likely derives from arrested or delayed SCPs differentiation towards the sympathoadrenal lineage[6], or immature sympathoadrenal progenitors that reacquired NCC/SCP-characteristics[18,21–23]. However, exact knowledge on the developmental origin, plasticity, and

treatment effects of NCC-related cancers including neuroblastoma, is currently lacking[14,24].

While animal models provide valuable insights into the aforementioned mechanisms[2,6,13,14,21,23], interspecies discrepancies impede recapitulation of all human-specific aspects of disease and development. These discrepancies include 1) developmental time scale[25,26] 2) gene expression in NCC/SCP derivatives, like reversed CART expression in human chromaffin cells and mouse sympathoblasts[14], 3) developmental mechanisms, including reversed fate transitions of the sympathoadrenal lineage[14], and 4) pathogenesis, such as missing metastasis[27,28]. Furthermore, while murine models recapitulate some aspects of the pathology, neuroblastoma does not naturally occur in mice[14,23,29,30].

Human pluripotent stem cell- (hPSC)based *in vitro* models (stembryo[31]) gained popularity as a human model, as it allows high-throughput screens[32–36], easy genetic modifications[32,37] and reporter-based lineage tracing[38–41], circumventing ethical constraints of human embryo use[25]. Current human stembryos include organoids of the posterior neural tube[32], elongating multi-lineage organized (EMLO) organoids of all three germ layers (gastruloids)[42], organoids of the trunk region including somites (somitoids)[43] and human-embryo like structures resembling human Carnegie stage (CS) 7 gastrula[44]. In this study, EMLO gastruloids are employed as a model of SCPs cell fate decisions, based on their displaying of central- and peripheral nervous system (PNS) components including putative NCCs and presumed nerve-associated SCP[35].

Due to their resemblance to embryonal posterior regions (human CS 8-9, mouse CS 8.5), stembryos have been used to model early mammalian symmetry-breaking, axis-formation, and organogenesis[32,35,36,42,45,46] as well as human-specific aspects of disease[47]. However, the field faces challenges of high phenotypic variability within experiments[31,46], repeatability, and reproducibility, often attributed to specific affordances of cell lines, batch effects of culture material, and differences between manufactureres[48]. To minimize variability, stembryo-culture requires tight control of 1) cell source[49] and pluripotency state[46,50], 2) matrix materials[43,51], 3) physical cues (e.g. culture density and

aggregate size)[32,36] and 4) spatiotemporal and dose of exogenous soluble factors such as growth factors (GF) and small molecule inhibitors/activators, most prominent of all *Wnt*-agonist CHIR[32,37,49,52].

As such, while stembryos can achieve physiological relevance by mimicking specific features of *in vivo* development, they require careful consideration of experimental needs, choice of model system, stringed quality tests of source material, and protocol optimization. Thus, this thesis aims to 1) choose a suitable cell line out of two commercially available cell lines ShiPS-miFF1 and STAN062i-164-2 for generation of EMLO gastruloids, 2) adapt EMLO gastruloid protocol, one of two currently available models of PNS development[35,53], into a model of neural crest lineage development, and 3) meticulously characterize the model and its cell types to ensure bioequivalence to human development.

Methods

Human induced pluripotent stem cells (hiPSC) and culture conditions

hiPSC lines ShiPS-miFF1 (MIFF) and STAN062i-164-2 (STAN) obtained from neonate, male Caucasian donors maintained were expanded on human ESC matrigel (Corning, 1:100 dilution) coated culture-ware in pluripotency media TeSR E8 (Stemcell Technologies) or mTeSR Plus (Stemcell Technologies) at 37°C and 5%CO_2. Media was exchanged every day for TeSR E8 and every second day for mTeSR Plus, and zones of differentiation were manually removed with every media change. Cultures were routinely passaged (split ratio 1:8) at 70-80% confluency, using EDTA solution (0,5mM, Sigma) in dPBS (Gibco) and gentle pipetting for STAN and ReLeSR (Stemcell Technologies) for MIFF iPSC.

EMLO gastruloid formation

EMLO gastruloids were generated following the “EMLO gastruloid protocol” described by the authors Olmsted and Paluh using hiPSC lines MIFF and STAN maintained to 60% confluency as starting material. For pre-treatment, multipotency media was replaced with N2B27 basal medium (1:1 Neurobasal medium (Thermo Fisher) DMEM/F12 (Corning), 2% B-27 Plus supplement (Thermo Fisher, 12587-010), 1% N-2 supplement (Thermo Fisher), 1x GlutaMAX (Thermo Fisher), 1x MEM Non-Essential Amino Acids (Thermo Fisher)) and supplemented with 3µM CHIR (StemCell Technologies) and 40ng/mL FGF2 (StemCell Technologies), unless indicated otherwise.

Colonies were maintained in pre-treatment medium for 2 days and media was changed daily. Aggregation protocol was started (day 0) by generation of a single cell suspension using 1:1 accutase (StemCell Technologies)/HBSS (Ca++ and Mg+ free, Gibco) and manual titration. All culture ware was coated with anti-adherence rinsing solution (StemCell Technologies), followed by two rinses with HBSS. Cell numbers were determined using Neubauer Counting Chamber, resuspending 10^6 cells/mL N2B27 supplemented with FGF-2 (10ng/mL), IGF-1 (2ng/mL, Miltenyi Biotec), HGF (2ng/mL, Miltenyi Biotec) and

Y-27632 (50 µM, StemCell Technologies). Cell suspension was maintained for 24h on an orbital shaker (75rpm, clockwise) in a humidified incubator (37°C, 5% CO_2).

On 1 and 2dsc, half of the media was swapped for N2B27 basal medium supplemented with FGF2 (10ng/mL), IGF1 (2ng/mL), and HGF (2ng/mL). On day 3 the entire volume of medium was exchanged for N2B27 basal medium supplemented with IGF1 (2ng/mL) and HGF (2ng/mL). On day 4 the EMLO all organoids were transferred to 100mm petri dishes treated with anti-adherence rinsing solution and maintained in N2B27 basal medium in a humidified incubator (37°C, 5% CO_2) on the orbital shaker (70rpm, clockwise). One-half of the medium was swapped every 3-4 days. For all experiments, repeatability was ensured by stringent control of initial iPSCs seeding density and cell number of single-cell suspensions during gastruloid generation.

Whole Mount Immunohistochemistry and clearing

EMLO gastruloids were pooled and fixed with 4% paraformaldehyde (PFA) solution for 2-6 hours depending on size at 4°C rocking. Samples were permeabilized by three consecutive steps of incubation (20 minutes, 4°C) in 0,2% TritonX-100 (Sigma) in 1x PBS (Gibco) and blocked overnight using 1% bovine serum albumin (BSA, Sigma) in 0,1% Tween20 (Sigma) in PBS (PBST). Gastruloids were transferred to 0.5mL epis and primary antibodies were added and incubated for 48 hours at 4°C (for dilutions and a listing of used antibodies see Table 1). Following incubation with primary antibodies, gastruloids were washed three times in 1% BSA in PBST and three times in PBST, before adding secondary antibody solution (1:1000) with nuclei staining with DAPI, 1ug/mL and incubating overnight at 4°C (for list of used antibodies see table 2). Incubation was followed by three washes in 1% BSA in PBST and 2 washes with PBST. Clearing was performed after dehydration in an ascending Methanol series (5 min 50% MeOH in PBS, three times 20 min in 100% MeOH) by using BABB. Images were taken with Zeiss LSM880 laser-scanning microscope (10x, 20x objective and 40x objective).

Immunohistochemistry

Samples were incubated overnight in 30% sucrose at 4°C, after which sucrose was removed and gastruloids embedded in OCT mounting media (StatLab). Samples were sectioned (14µm) on Superfrost plus slides and dried at room temperature for a minimum of one hour before staining. Alternatively, sections were stored at -20°C. For antigen retrieval before immunohistochemical staining, slides were submerged in target retrieval solution (DAKO) and steamed for 20 minutes. Slides were allowed to cool at room temperature for 40 minutes, before three washing steps (10min) in 0,1% Tween20 (Sigma) in 1xPBS (Gibco) (PBST). Samples were blocked in 3% normal donkey serum in 0,1% TritonX-100 (Sigma) in PBS before incubation in primary antibody solution (for dilutions and a listing of used antibodies see Table 1) in a humidified chamber at room temperature. Before secondary antibodies (1:1000) with additional nuclei staining with DAPI, 1ug/mL in 1x PBST was added (see table 2), and samples were washed three times (10min) in PBST. Secondary antibody incubation lasted for 90 minutes at room temperature, followed by three washes (10 minutes) with PBST. The gastruloids were mounted with Mowiöl mounting medium (Millipore). Images were taken with Zeiss LSM880 laser-scanning microscope (10x, 20x, 40x objective N/A).

Table 1: Primary antibodies

ANTIBODY	HOST	SECTION	WHOLE MOUNT	MANUFACTURER	IDENTIFIER
ALPHA-HAND2	rabbit	1:500		Abcam	ab200040
ALPHA-ISL1	mouse	1:200	1:150	hybridoma bank	39.4D5
ALPHA-P75/NGFR	rabbit	1:1000		Cell signaling	8238
BRN3A (POU4F1)	rabbit	1:300		Merck millipore	AB5945
CART	rabbit	1:1000		Phoenix Pharmaceuticals	H-003-62
FOX2A	goat	1:400	1:100	R&D Systems	AF2400
GATA6	goat	1:500	1:200	R&D Systems	AF1700
HSOX10	Goat	1:1000	1:800	R&D Systems	AF2864
HUC/D	mouse	1:500		Molecular Probes	A21271

PHOX2B	goat	1:1000	1:400	R&D	AF4940
SOX10	mouse	1:500		Santa cruz	sc-374170
SOX2	rabbit	1:1000	1:650	Abcam	ab97959
SOX8	rabbit	1:500		Gene Tex	GTX129949
TFAP2A (AP2 ALPHA)	mouse	1:50		Novus	NBP2-52571
TH	rabbit	1:1000	1:800	Sigma	T2928
TH	Sheep	1:500		NOVUS(bio)	NB300-110
TUJ1	mouse	1:500	1:400	Promega	G712A

Table 2: Secondary Antibodies

ANTIBODY	WAVELENGTH (NM)	CATALOG NUMBER	MANUFACTURER	HOST
ANTI-GOAT IGG	647	A21447	Thermo Fisher Scientific	donkey
	555	A21432	Thermo Fisher Scientific	donkey
	488	A11055	Thermo Fisher Scientific	donkey
ANTI-MOUSE IGG	647	A31571	Thermo Fisher Scientific	donkey
	555	A31570	Thermo Fisher Scientific	donkey
	488	A21202	Thermo Fisher Scientific	donkey
ANTI-RABBIT IGG	647	A-31573	Thermo Fisher Scientific	donkey
	555	A-31572	Thermo Fisher Scientific	donkey
	488	A21206	Thermo Fisher Scientific	donkey

Statistical analysis and acquisition of size parameters

Raw data was collected in Microsoft Excel *version 2309* (Build 16827.20130). Statistical tests were performed on multiple independent replicates using RStudio *2022.02.3* (Build *492*). Measurements of size parameters length (long axis of the organoid) and width (short axis of the gastruloid) were attained using Fiji software (aspect ratio: line tool; area: freehand selection tool) on bright-field images (PNG). Nuclei were automatically counted using Imaris based on

immunofluorescent images using Z-slices. ***p < 0.001, **p < 0.01, *p < 0.05, n.s. not significant (α = 0.05). Analysis of statistical power was not performed. More detailed information on the specific test used is provided in the figure legends of the results section.

Results

Cell-line-specific variations of morphology and gene expression during gastruloid formation

To model NCC lineage cell fate decisions, I adapted an existing gastruloid formation protocol by Olmsted and Paluh[35] (Figure 1A) using commercially available human iPSC lines ShiPS-miFF1 (MIFF) and STAN062i-164-2 (STAN) obtained from neonate, male Caucasian donors. This gastruloid protocol is divided into initial induction of two-dimensional (2D) iPSC colonies, followed by further aggregate formation and maintenance in three-dimensional (3D) suspension culture. In the following sections, time will be assigned as “days in suspension culture” (dsc) rather than “days *in vitro*”, to allow easier comparison with similar gastruloid protocols. Within suspension culture, various indicators of successful gastruloid development are employed: a) the overall increase in size, b) unidirectional elongation, and c) the formation of two compartments with distinct transparency[35].

To assess these parameters I measured aggregate area and aspect ratio from phase-contrast microscopy images (Figure 1B-C) during the “critical growth period” of the gastruloids, corresponding to 4- to 15 dsc[35]. Here, STAN- and MIFF-derived gastruloids, display an increase in their aspect ratios between 4- and 15 dsc, indicating successful elongation (Figure 1D, E). During the same timeframe, no significant increase in area was measured in either gastruloid culture (Supplementary Figure 1A, B), suggesting gastruloid elongation and overall size increase as independent mechanisms. This notion is further supported by a lack of correlation between size and elongation in gastruloids derived from both cell lines (Figure 1F). Of note, while at 4 dsc, MIFF-derived gastruloids presented significantly bigger areas (Supplementary Figure 1C) and higher aspect ratios (Figure 1G) than STAN-derived gastruloids their size was found to be almost identical at the end of the critical growth period (Figure 1F,

Supplementary Figure 1C). This agrees with measurements of gastruloid area, which continuously increase in STAN-derived gastruloids, while they stagnate at 4 dsc in MIFF-derived gastruloids (Supplementary Figure 1A). Taken together, these observations suggest a possible developmental retention of MIFF-derived gastruloids after 4 dsc.

Previous studies established that symmetry breaking within 72-96 hours of gastruloid formation sets up the anterior-posterior axis[35,36,42,46]. Symmetry breaking is characterized as polarized expression of early developmental TFs including BRACHYURY, SRY-box2 (SOX2), SRY-box1 (SOX1), and caudal type homeobox 2 (CDX2) by the posterior-, and GATA binding protein 6 (GATA6) within the anterior domain[35,36,42,46]. To assess the success of symmetry breaking of EMLOs generated from STAN- and MIFF iPSC, immunofluorescence analysis of samples after 4 dsc for expression of naïve pluripotency and neuroectodermal marker SOX2[54] and early mesoendodermal marker GATA6[36] was performed (Figure 1H). Quantification of gastruloid expression pattern, reveals that STAN-dervided gastruloids are significantly less likely to express SOX2 and undergo successful symmetry breaking than MIFF-derived gastruloids (Figure 1I). Halve (51%) of $SOX2^+$ MIFF-derived gastruloids show SOX2 immunoreactivity at the gastruloid core (centre) similar to murine gastruloids described by Suppinger et al. (2023), rather than secluded to one pole (49%) (Figure 1J). The lack of SOX2 immunoreactivity in STAN-derived gastruloids is puzzling, considering literature describing the default state of gastruloids before symmetry breaking as $SOX2^+$ aggregate[35,42].

Based on this analysis of morphological features and gene expression at the first 4 dsc of gastruloid formation, I hypothesize that 1) gastruloid elongation and growth are independent mechanisms, 2) iPSC lines diverge in likelihood of symmetry breaking events with STAN cell line failing to replicate early SOX2 expression.

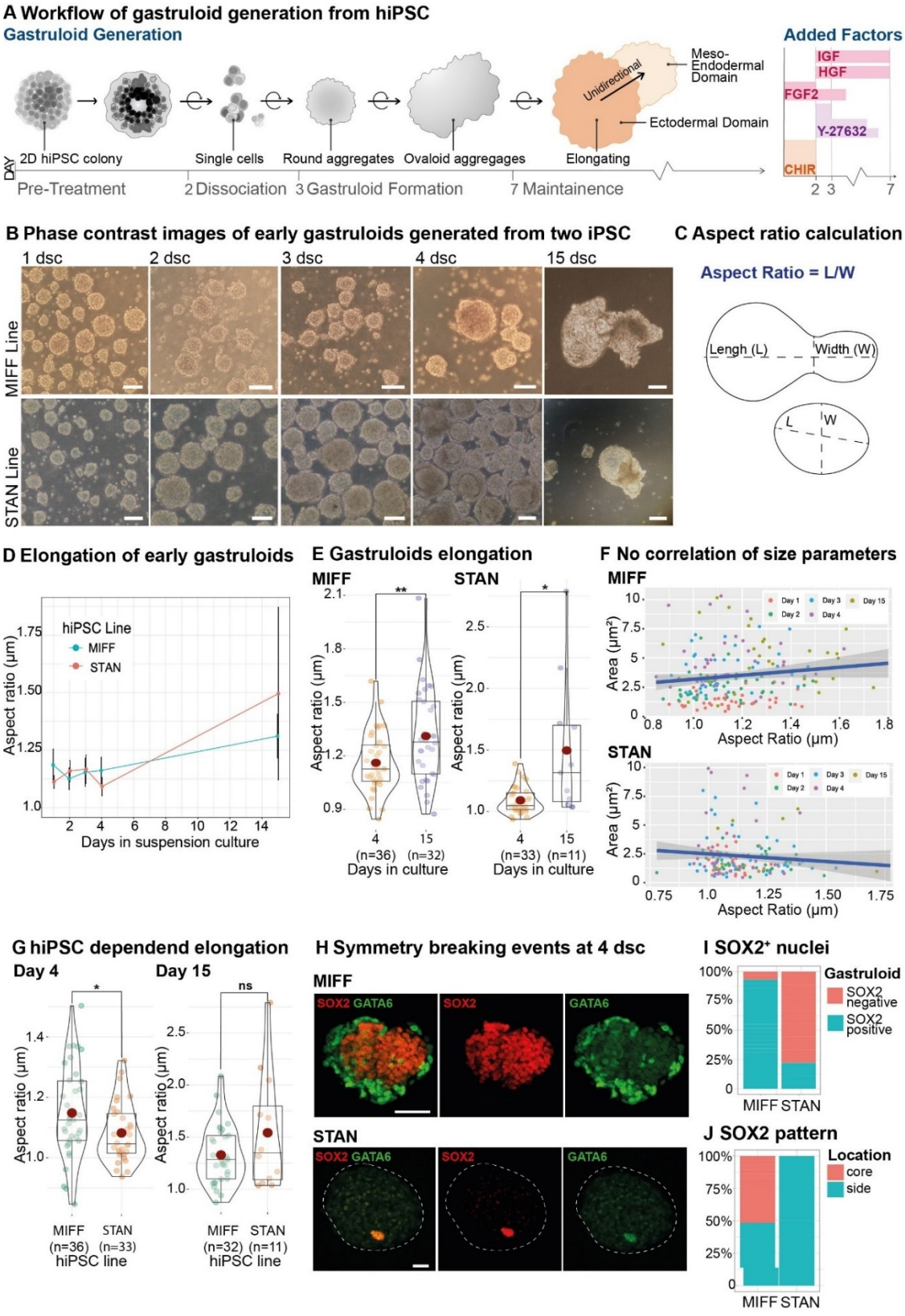

Figure 1: iPSC line affects the success of gastruloid protocol as defined by unidirectional elongation and early symmetry-breaking events of SOX2 and GATA6 expression*. (A) Schematic of gastruloid generation based on protocol published by Olmsted and Paluh (2021) (B) Phase contrast image of iPSC lines MIFF and STAN cultured in N2B27 for 15 dsc. Scale bars: 100 µm. (C) Schematic of gastruloids' aspect ratio measurement. Width measures the thinnest part of the gastruloid. (D) Linear regression of elongation of gastruloids generated from MIFF- and STAN- iPSC lines measured by aspect ratio between 1 and 15 dsc. (E) Violin plot showing MIFF- and STAN-derived gastruloids aspect ratios,*

*Student t-test p-value - * < 0.05, ** < 0.01,***<0.001, ns > 0.05, n is the number of quantified gastruloids per group. (F) Violin plot comparing MIFF- and STAN-derived gastruloids aspect ratio on 4 and 15 dsc by Student t-test p-value - * < 0.05, ** < 0.01,***<0.001, ns > 0.05, n is the number of quantified gastruloids per group. (G) Correlation of Area (measurements to the power of 104) and Aspect ratio of MIFF- and STAN-derived gastruloids throughout the 15 dsc. Datapoints are color-coded according to the day of measurement. (H) Immunofluorescence staining images of gastruloids derived from MIFF and STAN iPSC on 4 dsc showing SOX2 (red) and GATA6 (green). Scale bars: 20 µm. (I) Percentage of gastruloids with SOX2-positive cells (J) Percentage of gastruloids with SOX2-positive cells located in the core or on the periphery.*

Adjustment of culture conditions promotes elongation and rescues early symmetry breaking of STAN-derived gastruloids

Broad variability in the differentiation potential of hiPSC lines[52] requires cell line-specific adjustment of culture media[32,42], WNT agonist CHIR 99021 (CHIR)[32,37,42] and growth factor (GF) concentrations[46] to optimize elongation and symmetry breaking within established gastruloid protocols. Subsequently, I investigated the effects of culture media and GF concentrations on STAN-derived gastruloids at 4 dsc (Figure 2A-C; Supplementary Figure 2A, B) by comparison of control conditions (E8 media, 1xGF) with condition 1 (mTESRplus media, 3xGF), condition 2 (mTESRplus media, 1xGF) and condition 3 (E8 media, 3xGF). Data show that heightened GF conditions (conditions 1, 3) presented with an increased likelihood of gastruloids expressing SOX2 (Figure 2A, B) and a significant increase in aspect ratios (Figure 2C), but not organoid size (Supplementary Figure 2B), indicating GF-mediated promotion of SOX2 expression and elongation.

To examine STAN-cell line-specific effects of WNT-activation at 4 dsc, I applied variable concentration of the WNT agonist CHIR during initial induction of 2D iPSC colonies (3.0µM, 3.3µM, and 3.6µM) in combination with 3xGF concentrations (Figure 2C-H). Assessment of gastruloid morphology revealed two visually distinguishable compartments (Figure 2D), and a significant increase in aspect ratios of gastruloids subjected to 3.3µM, and 3.6µM CHIR (Figure 2F). Immunofluorescence-based (Figure 2E) quantification of gastruloids containing $SOX2^+$ cells, revealed significant variations between conditions, with 3.6µM CHIR conditions exhibiting SOX2 immunoreactivity in all assessed gastruloids (Figure 2G). Similarly, the number of $SOX2^+$ cells within gastruloids subjected to 3.6µM CHIR (mean 134 nuclei/gastruloid) were significantly higher than in gastruloids of 3.0µM (mean: 6 nuclei/gastruloid) and 3.3µM (mean: 21 nuclei/gastruooid) conditions (Figure 2I). In contrast to SOX2

expression, the number of GATA6^{+} cells does not seem to be affected by changes in CHIR concentration (Figure 2H). Notably, a new phenotype of two SOX2^{+}poles was observed in gastruloids of 3.6µM CHIR (Figure 2E), suggesting 3.6µM as the maximum CHIR concentration suitable for generation of unidirectionally elongating STAN-derived gastruloids. Additional experiments applying variations in CHIR- (3.0µM, 3.3µM) and GF-concentrations (1xGF, 3xGF) do not show combinatory effects of CHIR and GF on gastruloid morphology (Supplementary Figure 3A-G).

I failed to immunohistochemically detect the presence of neuroectodermal marker SOX2 and pan-neuronal marker neuron-specific class III beta-tubulin (TUJ1) positive fibers in STAN-derived EMLOs collected after 16 dsc (Supplementary Figure 3H). Overall, these data indicate that heightened CHIR- and GF-concentrations rescue 1) SOX2 expression and thus symmetry breaking, 2) morphological features of generation of two distinct domains and elongation of STAN-derived gastruloids during the first 4 dsc. However, generated organoids fail to form neuroectodermal derivatives making them unsuitable as a model for NCC and SCP lineage decisions.

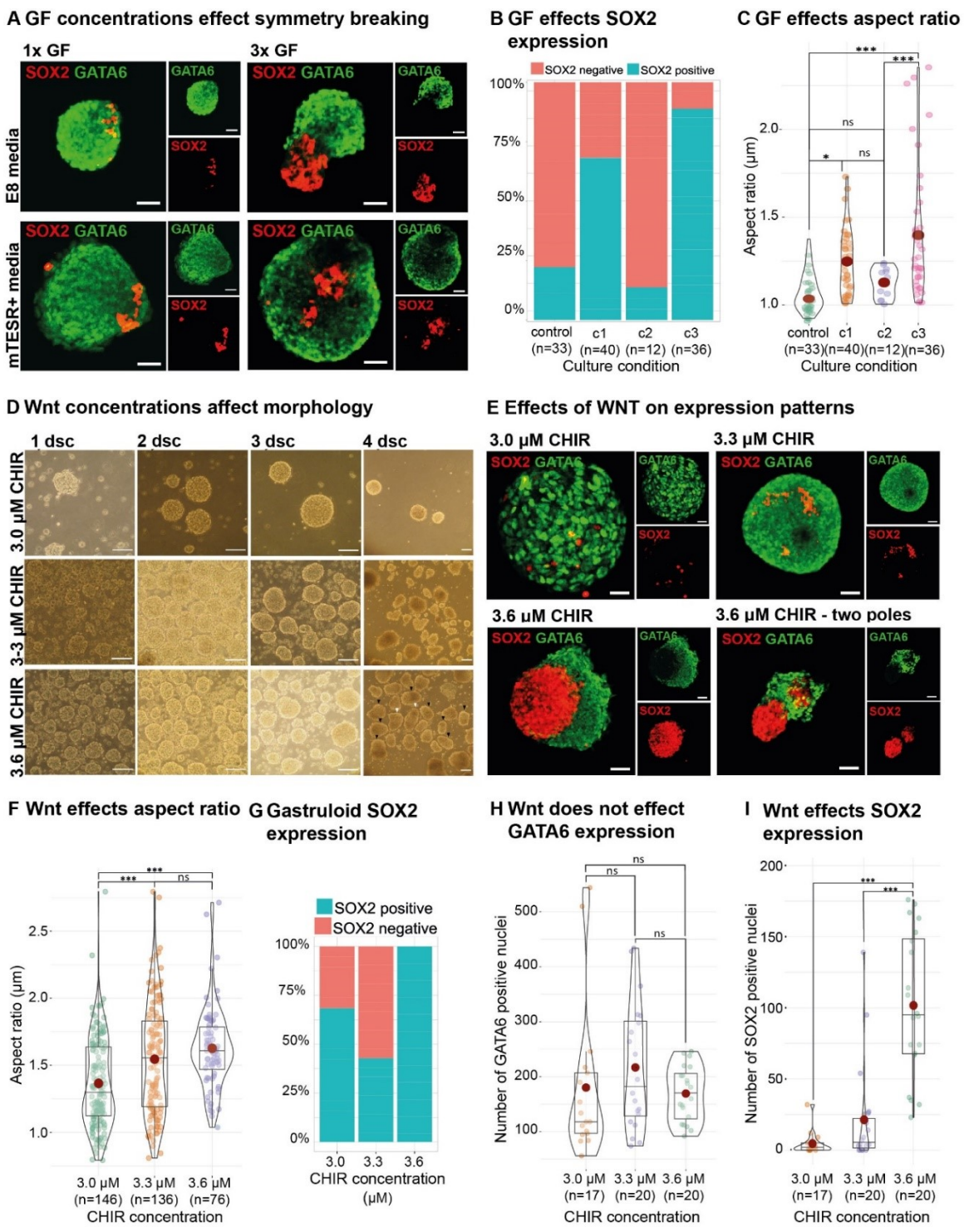

Figure 2: Culture conditions affect early gene expression and morphological characteristics of STAN-derived gastruloids. *(A) Immunofluorescence staining images of gastruloids derived from STAN iPSC on 4 dsc showing SOX2 (red) and GATA6 (green). Gastruloid starting material was cultured in either rich (mTESTplus) or poor (E8) media and gastruloids were either submitted to 1x (control) or 3x GF concentrations. Scale bars: 20 µm. (B) Percentage of gastruloids with SOX2-positive cells. (C) Violin plot showing STAN-derived gastruloids aspect ratio on 4 dsc comparing effects of media E8 and mTESRplus and GF concentration. A comparison of aspect ratios was done using Welch-ANOVA, p-value - * < 0.05, ** < 0.01,***<0.001, ns > 0.05. n is the number of quantified gastruloids per group. (D) Phase contrast image of STAN-derived gastruloids cultured in N2B27 for 4 dsc. Starting material was induced by either 3.0 µM, 3.3 µM, or 3.6 µM CHIR for 2 days. Black arrows indicate organoids with two domains (one darker, one lighter). White arrows indicate gastruloids with three domains. Scale bars: 100 µm. (E) Immunofluorescence staining images of gastruloids derived from STAN iPSC on 4 dsc showing SOX2 (red) and GATA6 (green). Starting material was induced by either 3.0 µM, 3.3 µM, or 3.6 µM CHIR for 2*

*days. Scale bars: 20 µm. (F) Violin plot comparing STAN-derived gastruloids aspect ratio on 4 dsc showing effects of CHIR concentrations on elongation of gastruloids. Comparison of aspect ratios was done using Welch-ANOVA p value - * < 0.05, ** < 0.01,***<0.001, ns > 0.05. n is the number of quantified gastruloids per group. (G) Percentage of gastruloids with SOX2-positive cells on 4dsc. Groups were subjected to 3.0 µM, 3.3 µM, or 3.6 µM CHIR. (H) Violin plot comparing effects of CHIR concentrations on the number of GATA6 expressing nuclei on 4 dsc in STAN-derived gastruloids. A comparison of aspect ratios was done using Welch-ANOVA, p-value - * < 0.05, ** < 0.01,***<0.001, ns > 0.05, n is the number of quantified gastruloids per group. (I) Violin plot comparing effects of CHIR concentrations on the number of SOX2+ nuclei on 4 dsc in STAN-derived gastruloids. A comparison of aspect ratios was done using Welch-ANOVA, p-value - * < 0.05, ** < 0.01,***<0.001, ns > 0.05, n is the number of quantified gastruloids per group.*

Prolonged Wnt induction rescues MIFF-derived gastruloids

Previous experiments (see "Cell-line-specific variations of morphology and gene expression during gastruloid formation") successfully reproduced unidirectional elongation and SOX2 and GATA6 symmetry breaking in MIFF-derived gastruloids but failed to replicate the extent of elongation and visible compartmentalization of conventional gastruloid protocols[35]. Literature indicates Wnt-activation post-aggregation as means to promote elongation in murine-[36,46] and human gastruloids[32,37] likely via regulation of induction, maintenance, and differentiation of neuromesodermal progenitors (NMPs, characterized by the marker SOX2)[37,43,55,56]. Subsequently, I prolonged CHIR induction for 1 dsc (+1 day), 3 dsc (+3 days), and 7 dsc (+7 days) and assessed its effects on previously defined parameters of successful gastruloid formation (Figure 3A).

Prolonged Wnt conditions (+7 days) successfully rescued gastruloids compartmentalization into putative mesoendodermal- (light) and ectodermal (dark) domains as determined by visual assessment via phase contrast microscopy (Figure 3B, Supplementary Figure 4A). Furthermore, prolonged CHIR exposure promoted elongation but not growth past 4 dsc, as indicated by significantly higher aspect ratios, but not areas in gastruloids subjected to prolonged CHIR induction on 16dsc (Figure 3C). Fitting the hypothesis of retained development past 4dsc, aspect ratios do not differ significantly between treatment groups at 4 dsc (Supplementary Figure 4B), and aspect ratio but not area of gastruloids subjected to prolonged CHIR, increase drastically within the critical growth period (Supplementary Figure 4C). Additionally, comparison gastruloids at 4 dsc and 16 dsc showed a significant increase in area but not aspect ratios in control conditions, while gastruloids subjected to prolonged CHIR induction showed a significant increase in both area and aspect ratios (Supplementary Figure 4D).

Effects of Wnt signaling on SOX2 and GATA6 induction was assessed by whole-mount immunochemistry on 2 dsc, 4 dsc, and 7 dsc (Figure 3D) and compared between groups (Figure 3E) and time points (Supplementary Figure 5). Here, the number of $SOX2^+$nuclei per gastruloid at 7 dsc was significantly higher in groups with long CHIR induction (+3 days, +7 days) than in gastruloid submitted to shorter periods (+1 day) of CHIR (Figure 4E). Furthermore, the number of $SOX2^+$ nuclei increased with time in long- (+3 days and +7 days) but not in control and +1day CHIR induction periods (Supplementary Figure 5A). While the comparison of time points shows an overall increase of $GATA6^+$ nuclei with time in all treatment groups (Supplementary Figure 5B), no treatment group-dependent trends in the number of $GATA6^+$ nuclei were found (Figure 4E).

Recently, Suppinger et al (2023) described the asynchronous development of gastruloids as a hurdle in the statistical analysis of treatment effects on morphology and gene expression[46]. Accordingly, I analyzed the possible correlation between the number of $SOX2^+$ and $GATA6^+$ nuclei and the length of CHIR induction independent of time. Here I show, that whilst measurements of separate time points did not reveal a significant trend, time-independent analysis shows a positive correlation of both SOX2 and, surprisingly GATA6 expression with the length of CHIR exposure (Figure 3F). Together these data suggest extended Wnt induction as a key aspect in achieving desired morphology, size parameters, and heightened expression of SOX2 and GATA6 in gastruloids generated from MIFF hiPSC.

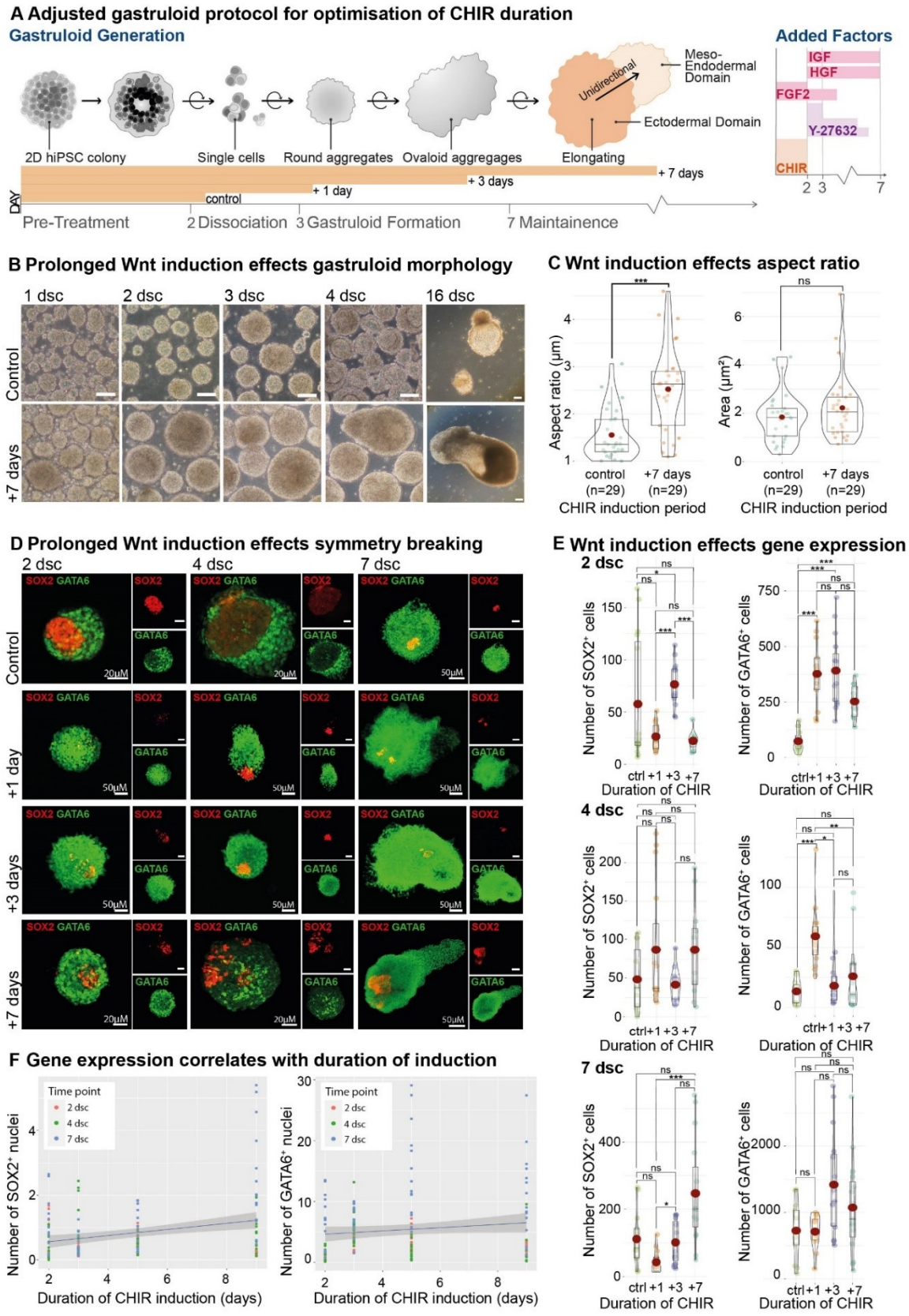

Figure 3: Effects of duration of WNT-activation on MIFF-derived gastruloids. *(A) Schematic of the experimental setup of gastruloid generation with different durations of WNT-activation by WNT-agonist CHIR. (B) Phase contrast image of MIFF-derived gastruloids cultured in N2B27 for 16 dsc. iPSCs were induced for 2 days (control) in 2D culture, 2 days in 2D culture, and 7 dsc. Scale bars: 100 µm. (C) Violin plot showing MIFF-derived gastruloids aspect ratio and area (y-axis measurements to the power of 105) at 16 dsc, comparing effects of control and +7 days CHIR induction. Statistical analysis was done using*

*students' t-test p-value - * < 0.05, ** < 0.01,***<0.001, ns > 0.05. n is the number of quantified gastruloids per group. (D) Immunofluorescence staining images of gastruloids derived from MIFF iPSC on 2-, 4-, and 7 dsc showing SOX2 (red) and GATA6 (green). Starting material was induced for either 2 days (control) in 2D culture, or for 2 days in 2D culture and 1-, 3-, or 7 dsc. Scale bars: 20 µm. (E) Violin plot of the number of SOX2+ or GATA6+nuclei per gastruloid. Statistical analysis was done with Welch-ANOVA, p-value - * < 0.05, ** < 0.01,***<0.001, ns > 0.05. n is the number of quantified gastruloids per group. (F) Spearman correlation of the number of SOX2+ or GATA6+ nuclei and duration of CHIR induction in MIFF-derived gastruloids throughout 7 dsc. Datapoints are color-coded according to the day of measurement. Y-axis measurements to the power of 102*

Prolonged Wnt induction allows formation of the neural compartment and neural tube-like-structures in MIFF-derived gastruloids

To confirm MIFF-derived gastruloids' successful generation of a neural compartment as indicated by the formation of two visually distinguishable compartments upon prolonged CHIR exposure, the existence of a neural compartment in gastruloids subjected to prolonged CHIR exposure was validated by the existence of TUJ1^{+} cells on 7-, 16- and 20 dsc[57]. However, due to the high phenotypic heterogeneity of gastruloids sampled within time points (Supplementary Figure 6), developmental stages were inferred from the qualitative categorization of gastruloids according to 1) TUJ1 signal density, 2) neurite formation of TUJ1+ cells and 3) location of pan-neuronal maturation gene and NC/SCP marker P75-NGFR and set on a pseudo-time trajectory (Figure 4A).

As such I defined stage 1 (n=3) as mildly elongated gastruloids containing TUJ1^{+} positive cell bodies showing no/few short neurites that are proximal to a singular cluster of P75^{+} cells. Stage 2 (n=4) was characterized by a neural compartment consisting of TUJ1^{+} cell bodies including neurites, and a cluster of P75^{+} cells. Stage 3 (n=4) gastruloids show pronounced neural projections reaching from a neural compartment into a non-neural compartment and a set of P75^{+} cells attached to TUJ1+ projections. The average frequency of developmental stages was mapped back to time points to ensure the quality of defined developmental stages. Fittingly early gastruloids (7 dsc) predominantly classify as stage 1, whilst late gastruloids (16 and 20 dsc) are equally classified as stage 2 or 3. As such our gastruloids display neural markers, predominantly confined to one neuronal compartment, with increasing neuronal projections

extending toward a putative meso-endodermal compartments as gastruloids mature.

Previously data showed that prolonged CHIR exposure (+7 days) is sufficient to increase the number of SOX2-expressing cells in maturing gastruloids and induce levels of elongation comparable to those of other gastruloid models. Moreover, gastruloids subjected to prolonged CHIR exposure revealed cylindric SOX2^{+} structures reminiscent of a neural tube within the TUJ1^{+} neural compartment, that persisted from 7 dsc to 20 dsc. This assumption of a neural-tube-identity was further supported by co-expression of definitive endoderm and neural tube floor plate marker FOXA2 by a fraction of SOX2^{+} cells within the putative neural tube (Figure 4B). At the same time, the putative neural tube is often located close to pore-like structures and, covered by a cell layer with epidermal morphology at 20 dsc. This is in stark contrast to GATA6^{+}/FOXA2^{+} cylindric structures identified as primitive gut tube by Olmsted and Paluh (2021), however ties with neural tube formation previously described in mouse gastruloids at 4 dsc[51] and human peri-gastruloids at 11 dsc[58].

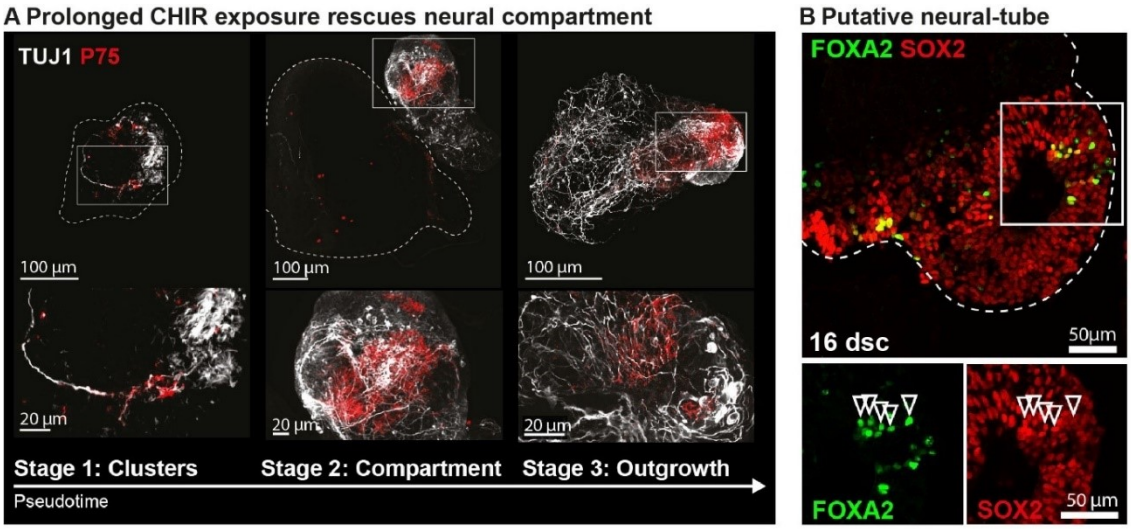

Figure 4: Presence of neural compartment in MIFF-derived gastruloids subjected to prolonged CHIR exposure*. (A) Representative immunofluorescent image-based pseudotime trajectory of nervous compartment development of MIFF-derived gastruloids cultured in N2B27. TUJ1 (white) and P75 (red). (B) immunofluorescent image of the putative neural tube in sections of gastruloids on 16 dsc. White arrows indicate SOX2 (red) and FOX2A (green) co-expressing nuclei.*

MIFF-derived gastruloids exposed to prolonged Wnt induction express markers of NCCs, SCPs, and their derivatives

Assessment of the potential of MIFF-derived gastruloids as a model for human NCC and SCP cell-fate decisions was based on the presence of 1) NCCs/SCPs and 2) NCC/SCP sensory- and autonomic derivatives including transitory states co-expressing markers of competing fates[6,13]. Gastruloids obtained by control conditions failed to yield a neural compartment and NCCs/SPCs as shown by lack of TUJ1$^+$, P75-NGFR $^+$ and SOX10$^+$ cells[2,13,14] on 7-, 16-, 34- and 41 dsc (Supplementary Figure 7A) and missing neural-tube-like structures indicated by SOX2$^+$ nuclei (Supplementary Figure 7B). Furthermore, they failed to display CART$^+$, TH$^+$, BRN3A$^+$, and PHOX2B$^+$ derivatives of NCC/SCP (Supplementary Figure 7 C-E), beyond stochastically occurring singular cells. Subsequently, they were deemed unfit as a model of human NCCs/SCPs cell fate decisions and will not be discussed further.

To identify putative NCC and SCP, MIFF-derived gastruloids were subjected to prolonged CHIR induction, kept in culture for up to 42 days, and were characterized by immunofluorescent staining of NCC markers SOX10, P75-NGFR, and TFAP2 (Figure 5A)[2,13,14] and proximity/association with TUJ1$^+$ nerves[35,59]. However, detection of SOX10 within whole mount samples returned poor quality stainings with low signal and high background. As a result, technical-, rather than biological causes of P75-NGFR$^+$/SOX10$^-$ cell clusters on 7 dsc cannot be ruled out and SOX10 staining was deemed inconclusive (Supplementary Figure 6). Analysis of gastruloids at 16 dsc revealed a population of TFAP2$^+$ putative NCCs (Supplementary Figure 9A).

Gastruloid samples collected at 34 dsc, revealed P75$^+$/SOX10$^+$ putative NCCs in proximity to drop-shaped structures morphologically resembling a neural tube or neuroectodermal-like structure (Figure 5B). Moreover, gastruloids starting from 20dsc up to 42 dsc additionally displayed P75$^+$/SOX10$^+$ SCP-like cells located near TUJ1$^+$ nerve fibers. To test whether this NCC model can be used to validate mouse data[13] in a human system, expression of the “hub” gene SOX8 was analyzed in day 34 gastruloids, discovering a SOX8$^+$/SOX10$^+$, non-nerve associated cell population in proximity to neural-tube-like structures (Figure 5C).

As such these findings establish MIFF-derived gastruloids as a model for human NCCs and SCPs cell-fate decisions by proving their capacity to produce freely migrating NCCs and nerve-associated migratory SCPs. Furthermore, this observation is the first to experimentally prove the existence of a SOX8^{+}/SOX10^{+} intermediate hub population within a human model system.

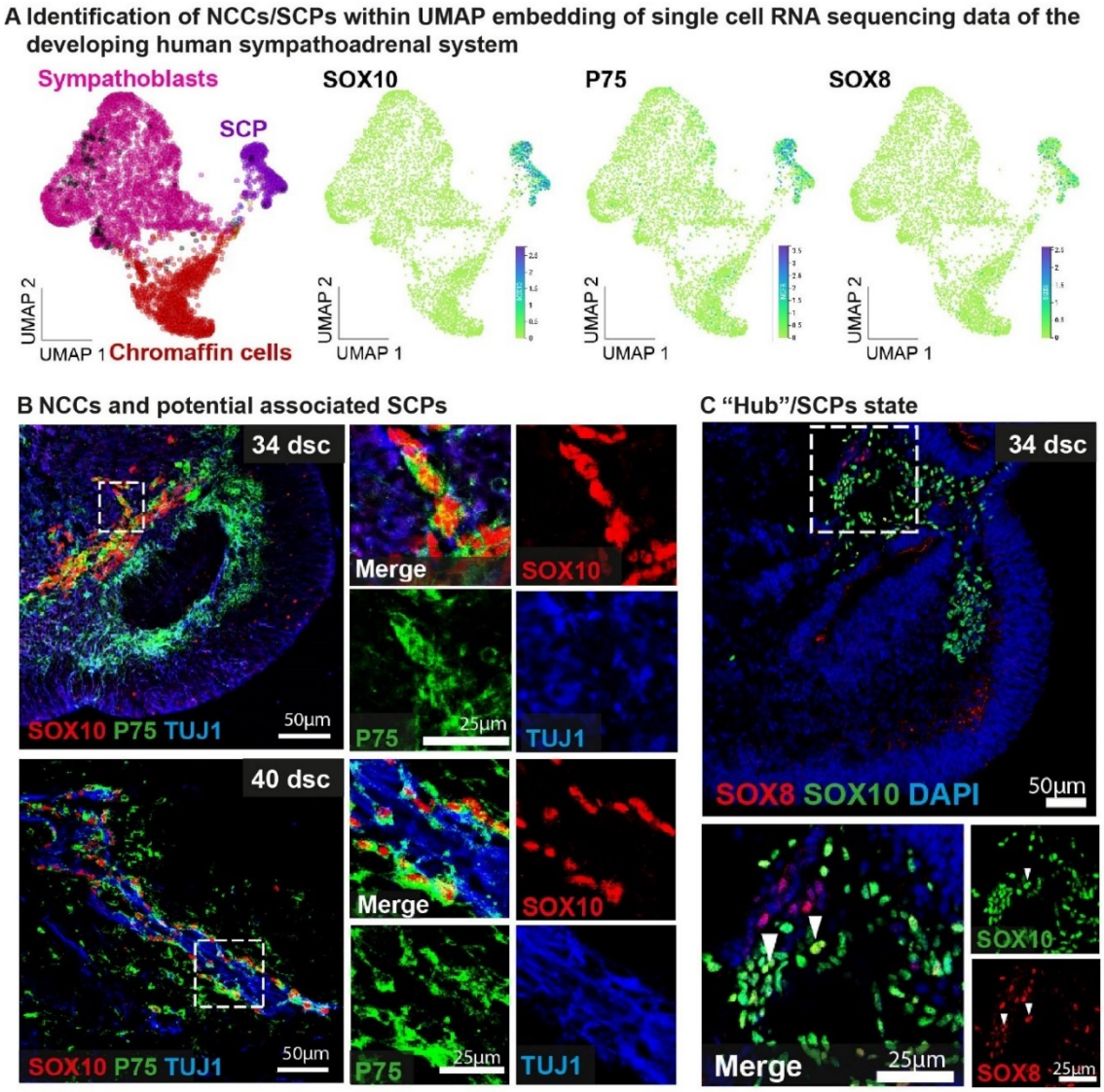

Figure 5: Presence of potential NCC and nerve-associated SCPs in MIFF-derived gastruloids subjected to prolonged CHIR exposure*. (A) NCC/SCP marker genes SOX10, P75, and hub-marker SOX8 UMAPP shown on UMAP embedding of RNA sequencing data of the developing human sympathoadrenal system generated by Kameneva et al. (2021). (B) Immunohistochemistry for SOX10 (red), P75 (green), and TUJ1 (blue) on sections of gastruloids at 34-and 41 dsc. (C) Immunohistochemistry for SOX8 (red) and SOX10 (green) of gastruloids at 34 dsc. Arrowheads indicate SOX8+/SOX10+ nuclei.*

To further explore the ability of this *in vitro* model to mimic *in vivo* fate decisions of NCCs/SCPs, I attempted to capture fate transitions and NCC/SCP derivatives focusing on the sympathoadrenal lineage by selecting markers from single-cell RNA sequencing-based studies of the developing human sympathoadrenal

system (Supplementary Figure 9B)[14]. ISL1^{+}/PHOX2B^{+}/TH^{+} sympathoadrenal biased progenitors were observed at 23-, 27-, 30-, and 34 dsc (Supplementary Figure 8) and categorized into developmental stages in pseudo time (Figure 6A). Stage 1 was defined by low-density, non-organized TH^{+}/PHOX2B^{+}/ISL1^{+} cell clusters, spatially segregated from ISL1^{+}/TH^{-}/PHOX2B^{-} compartments (n=8). Stage 2 was defined by heightened amounts of TH^{+}/PHOX2B^{+}/ISL1^{+} cells with long neurites in the proximity of ISL1^{+}/TH^{-}/PHOX2B^{-} clusters and the occurrence of ISL1^{+}/PHOX2B^{+}/TH^{+} ganglia-like-structures (n=6). Lastly, stage 3 is defined by a TH^{+}/PHOX2B^{+}/ISL1^{+} compartment including a pore-like structure that is opposite of an ISL1^{+}/TH^{-}/PHOX2B^{-} compartment that corresponds to potential mesodermal cardiac progenitors[60] (n=5).

Further inquiry into the reproduction of *in vivo* NCC lineage decisions included the identification of SCP-to-sympathoblast TFAP^{+}/ PHOX2B^{+}/TH^{+} transitory cell states, found within sections of gastruloids on 16 dsc (Figure 6B). Interestingly, while the existence of SCP-to-chromaffin cell SOX10^{+}/HAND2^{+} transitory cell states could not be verified in 20 dsc gastruloids (Figure 6C), they presented with SOX10+TUJ1+ neuronal cell bodies indicative of neuronal fate transitons[13,61]. Additional immunohistochemical analysis for mature NCC/SCPs-derived cell types on gastruloid sections, did not return TH^{+}ISL^{+}HAND2^{+} early sympathoblasts at 16- or 20 dsc (Supplementary Figure 9C), or BRN3A^{+}/TH^{+} sensory neurons on 7-, 16-, 27-, or 41 dsc (Figure 6E). However, a small fraction of CARTPT^{+}/TH^{+} chromaffin cells in 41 dsc gastruloids (Figure 6D) and putative SOX2^{+}/HUC/D^{+} (Figure 6F) in 16 dsc gastruloids were identified.

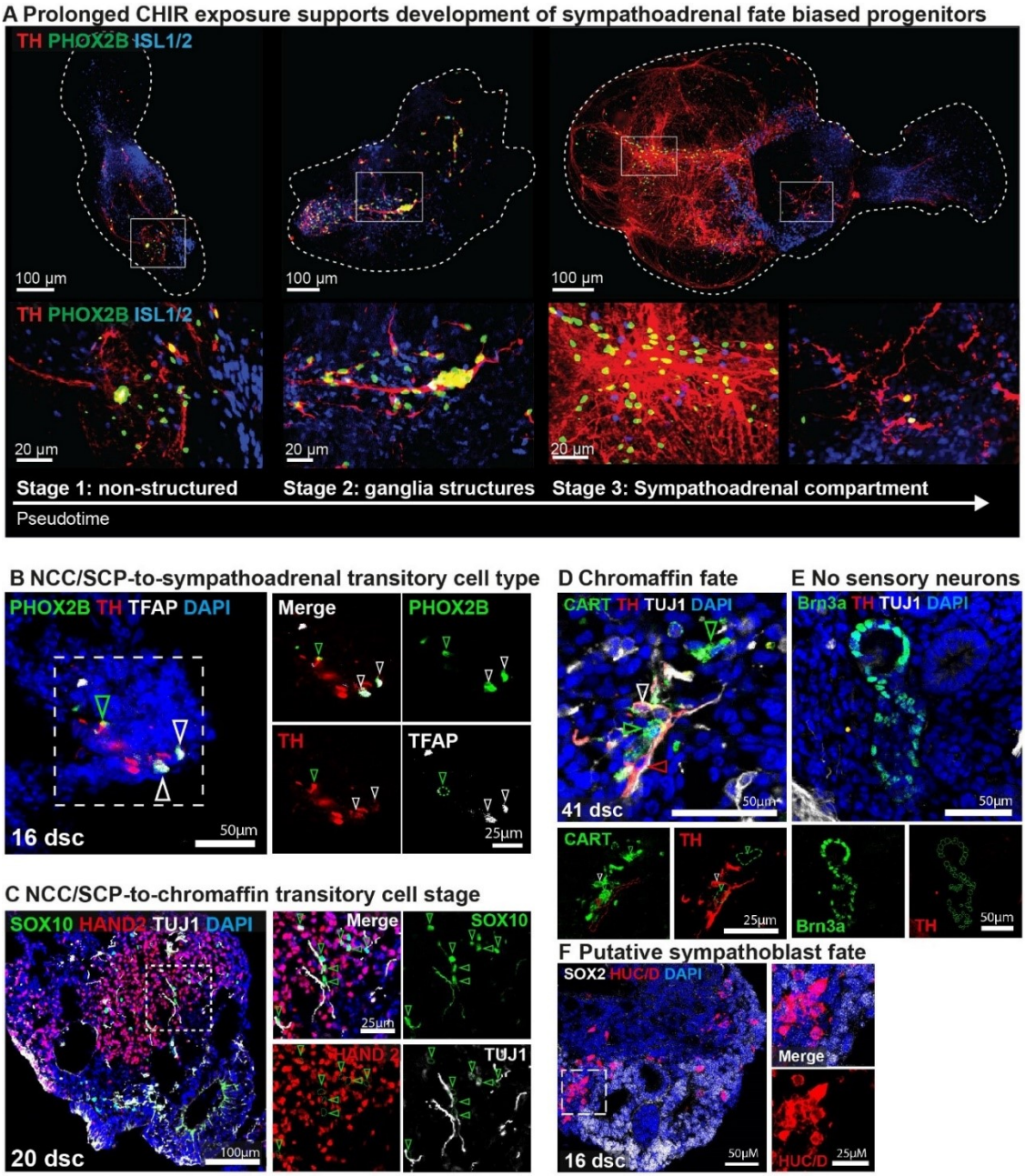

Figure 6: Presence of NCCs/SCPs lineage-derived cell types within MIFF-derived gastruloids subjected to prolonged CHIR induction. *(A) Representative immunofluorescent image-based pseudotime trajectory of generation of sympathoadrenal lineage staining for TH (red), PHOX2B (green), and ISL1/2 (blue). (B) immunofluorescent image of putative transitory cell states in sections gastruloids after 16 dsc. White arrowheads indicate PHOX2B (green), TH (red), and TFAP2 (white) co-expressing nuclei, green arrowheads indicate more mature derivatives that are PHOX2B and TH positive, but no longer express TFAP. (C) Immunohistochemistry for SOX10 (green), HAND2 (red), and TUJ1 (white) on sections of gastruloids at 20 dsc. Green arrowheads and outlines indicate nuclei. (D) Immunohistochemistry for chromaffin markers CART (green), TH (red), and TUJ1 (white) on sections of gastruloids after 41 dsc. Green arrowheads and outlines indicate $CART^{+}/TH^{-}$ cells. Red arrowheads and outlines indicate $CART^{-}/TH^{+}$ cells. White arrowheads indicate $CART^{+}/TH^{+}$ putative chromaffin cells. (E) Immunofluorescent image of sensory neuron markers Brn3a (green), TH (red), and TUJ1 (white) on sections of gastruloids after 41 dsc. Green outlines mark $BRN3A^{+}$ nuclei in the TH panel. (F) Immunohistochemistry for neuronal marker HUC/D (red), and SOX2 (white) on sections of gastruloids after 16dsc.*

Discussion

NCCs and their peripheral-nerve-associated derivatives, SCPs, have been intensely researched due to their developmental importance[1,2,6] and, more recently, involvement in pathologies such as melanoma, neurofibromatosis and neuroblastoma[11,14,15,17,23,62]. However, interspecies differences[14,25–28] and inaccessibility of human embryos[63] limit insights into human-specific aspects of NCC specification and downstream cell fate decisions. Following this reasoning, the present study aimed to adapt the published EMLO gastruloid protocol[35] as a human iPSC-based *in vitro* model of NCC lineage cell fate decisions, NCC clonality, and multipotency[64] (Figure 3A).

Adapted multilineage iPSC-derived organoids, form an extensive neural compartment including a neural tube-like-structure (Figure 4 A, B), followed by the emergence of early- (TFAP2a$^+$; Figure 5B, Supplementary figure 9A)[65,66] and late migratory NCCs (SOX10$^+$, NGF-P75$^+$; Figure 4D). Moreover, the model's potential to replicate early *in vivo* NCCs/SCPs lineage relationships was verified by the existence of nerve-associated SCPs (SOX10$^+$, NGF-P75$^+$; Figure 4D)[1,11,66] and transitory NCCs/SCPs belonging to the "hub" state (SOX8$^+$/SOX10$^+$; Figure 4E)[13,14,67] as early as 34 dsc. Detection of an early sympathoadrenal-biased cell population and later formation of NCC derivatives including mature autonomic neurons and chromaffin cells (Figure 5), indicates iPSC-multilineage organoids additionally replicate downstream cell fate specification of NCC/SCPs, reminiscent of *in vivo* differentiation of the sympathoadrenal lineage by NCCs/SCPs[7,68,69].

The discovery of early sympathetic differentiation independently of SCPs phenotype and late chromaffin cell occurrence after the detection of SCPs associated with nerves is in line with the timing of *in vivo* sympathetic and chromaffin lineage segregations. *In vivo*, sympathoblasts building sympathetic chain ganglia are known to derive from freely migrating NCCs[2] during CS 16/17[70] and SCPs from CS 18 onwards[13]. Chromaffin cells on the other hand require nerve-associated precursors and therefore develop later[14,70]. As such, early sympathoadrenal lineage-biased populations could descend from early migratory NCCs[2,70], rather than SCPs[14,71]. Nevertheless, as organoids lack the

embryonal morphology and thus migratory pathways, migration-dependent processes might be heavily altered within organoids. This may in turn result in alterations in developmental timing, or lineage relationships. Subsequently, characterization of the developmental timing of marker expression and cell types within this model requires further experimental appraisal based on optimized immunohistochemical protocols, and fluorescent reporter lines routinely used in organoid culture[39–41,46]. Additionally, transgenic cell lines allow verification of lineage relationships- and developmental timings-bioequivalence, by Cre-mediated lineage tracing[72,73], or CRISPR–Cas9 lineage tracing recorders[38,74]. Lastly, single-cell-omics methods, have been excessively used on organoid models[34,35,46,75] to analyze expression dynamics, characterise transition cell states, and deduct cell fate decisions in pseudotime. Furthermore, spatial transcriptomics could shed light on the spatial relationships of fate-biased cells. Therefore, they present a valuable alternative to characterize NCCs/SCPs lineage progression, similar to previous research on murine embryos[6] and the human sympathoadrenal system[14].

hiPSC-derived stembryos offer complex, accessible, high throughput modeling of cell fate decision making[53], self-organization[36], and organogenesis of the developing embryo[36,56,76,77] and human disease[47,78]. However, the field struggles with low reproducibility and the need for cell-line-specific optimization of exogenous biochemical factor Wnt-agonist CHIR within established stembryo protocols[31,35,37,42,51]. In this study, I hypothesize that observed cell line-specific heterogeneity in gastruloid generation of hiPSC lines MIFF and STAN is based on distinct WNT-mediated developmental mechanisms activated through CHIR. As such, symmetry breaking and activation of SOX2 expression in STAN-EMLO (Figure 1H, I) was rescued by increased CHIR- and FGF2 treatment (Figure 2), likely linked to early Wnt-activation directly by CHIR or indirectly by FGF2-mediated activation of endogenous Wnt signaling[79]. This is consistent with previous research on hiPSC and stembryos suggesting the key role of Wnt signaling in caudalization[42] and induction of SOX2 expression[52,56,80,81]. On the other hand, prolonged CHIR-induced Wnt-activation, rescued the formation of the neural compartment in MIFF-derived gastruloids (Figure 3, Supplementary Figure 6, 7), likely by stabilization[46] and increase of SOX2[32,37] expression and

enhancement of SOX2+ neuro-mesodermal progenitors (NMP) fate maintenance and decision making[34,36,37,46,56]. In line with others, I find that prolonged CHIR exposure of MIFF-derived gastruloids resulted in increased elongation[43,77], likely by adding to NMPs Wnt secretion, which has been shown to promote rearrangements of cells at the posterior end[37].

As such, our results suggest STAN- and MIFF cell line-specific requirements for activating factors are routed in two temporally segregated, Wnt-driven, developmental mechanisms, however, they do not explain cell lines diverging response to the methodology of the original protocol. As previous work by others suggests differentiation potential of iPSCs as basis for diverging performance in stembryo formation protocols[48,49,52,82], Veronika Fleischhart investigated the capacity of different cell lines to differentiate into the three germ layers ectoderm, mesoderm, and endoderm (trilineage potential). Consistent with the results of this thesis, STAN iPSCs had reduced potential to produce ectoderm, explaining diminished SOX2 expression, while the MIFF iPSC line shows slightly reduced potential to produce mesoderm, fitting our hypothesis of impaired NMP fate. Consequently, these data suggest cell line-specific requirements of biochemical factors during gastruloid formation to cell lines' inherent pluripotency. This further suggests that assessment of the trilineage potential of each source of iPSCs is a vital strategy to predetermine iPSC performance in stembryo culture and relevant fast-track optimization efforts.

State-of-the-art iPSC 2D models of guided NCC differentiation[83], micropatterned gastruloids[84], and chip-based models of the neural tube[85] allow insights into early NCC fate specification and early migratory mechanisms. However, they lack geometric-and mechanic complexity, and cell-cell and cell-matrix interactions provided in 3D culture. Recently introduced, neuro-mesodermal assembloids, model meso-ectodermal-interactions, and NCC induction and migration[35,53]. In choosing a self-organization-based stembryo model[35], rather than tightly controlled, more artificial model like neuro-mesodermal assembloids, the hereby introduced multilineage organoids allow for high cellular heterogeneity and recapitulation of *in vivo* development. For this reason, adapted multilineage organoids are a powerful tool for the investigation of molecular determinants that drive cell-fate decisions of NCC and

SCPs in high temporal resolution, allowing for easy manipulation of morphogenic principles leading up to SCP cell fate choices by selected morphogenic factors and signaling molecules. Furthermore, recent work showing that mechanical-pressure rescued *in vivo* tissue morphology[58,86,87] in mouse-[34,51] and human[43] organoids indicates promising future directions of generating morphologically accurate migratory environments of NCCs/SCPs [88,89] by the addition of extracellular matrix to this *in vitro* model of NCC lineage decisions.

Finally, faulty NCCs/SCPs lineage decisions have been linked to embryonic- and adult malignancies including melanoma[15,16], neurofibromatosis[17], and neuroblastoma[14,18,19,23]. Accordingly, the usage of cancer cell lines, or patient-derived iPSCs as starting material for organoid generation[78,90], might allow insights into novel aspects of NCC-derived tumors. Furthermore, easy accessibility of organoid models allows for transgenic tracking and genetic functional studies using viral vectors, inducible systems like TET-on[91], or CRISPR/Cas9 for targeted genomic mutations[32,37] of classic oncogenic pathways like MYCN or genes implicated in NCC/SCPs-derived tumors such as ALK receptor tyrosine kinase and sympathoadrenal biasing transcription factor PHOX2B implicated in hereditary neuroblastoma[23,62,92].

In summary, with this thesis I introduce an adjusted MIFF-derived multilineage organoid model, that serves as one of few 3D models of NCCs/SCPs decision making[35,53] by 1) displaying a neural compartment and neural tube-like-structures, 2) NCCs induction and nerve-association of SCPs-like cells, 3) expression of biomarkers of several stages of NCCs/SCPs including NCCs/SCPs hub state, sympathoadrenal bias and NCCs/SCPs mature derivatives, autonomic neurons and chromaffin cells. Furthermore, my experimental findings on MIFF- and STAN-derived organoids, suggest optimization of Wnt-activation intensity and timing based on consideration of iPSC lines pluripotency state. Lastly, I propose the usage of transgenic lines to aid this model's applicability as a disease model for NCC-derived pathologies like neuroblastoma.

References

1. Bronner, M.E., and Simões-Costa, M. (2016). The Neural Crest Migrating into the Twenty-First Century. Curr Top Dev Biol *116*, 115–134. 10.1016/bs.ctdb.2015.12.003.

2. Erickson, A.G., Kameneva, P., and Adameyko, I. (2022). The transcriptional portraits of the neural crest at the individual cell level. Seminars in Cell & Developmental Biology. 10.1016/j.semcdb.2022.02.017.

3. Gilbert, S.F. (2000). Formation of the Neural Tube. In Developmental Biology. 6th edition (Sinauer Associates), p. Chapter 12.

4. Rogers, C.D., and Nie, S. (2018). Specifying neural crest cells: From chromatin to morphogens and factors in between. Wiley Interdiscip Rev Dev Biol *7*, e322. 10.1002/wdev.322.

5. Rothstein, M., Bhattacharya, D., and Simoes-Costa, M. (2018). The molecular basis of neural crest axial identity. Developmental Biology *444*, S170–S180. 10.1016/j.ydbio.2018.07.026.

6. Soldatov, R., Kaucka, M., Kastriti, M.E., Petersen, J., Chontorotzea, T., Englmaier, L., Akkuratova, N., Yang, Y., Häring, M., Dyachuk, V., et al. (2019). Spatiotemporal structure of cell fate decisions in murine neural crest. Science *364*, eaas9536. 10.1126/science.aas9536.

7. Saito, D., Takase, Y., Murai, H., and Takahashi, Y. (2012). The dorsal aorta initiates a molecular cascade that instructs sympatho-adrenal specification. Science *336*, 1578–1581. 10.1126/science.1222369.

8. Kelsh, R.N., Camargo Sosa, K., Farjami, S., Makeev, V., Dawes, J.H.P., and Rocco, A. (2021). Cyclical fate restriction: a new view of neural crest cell fate specification. Development *148*, dev176057. 10.1242/dev.176057.

9. Gilbert, S.F. (2000). The Neural Crest. In Developmental Biology (Sinauer Associates), p. Chapter 13.

10. Krispin, S., Nitzan, E., Kassem, Y., and Kalcheim, C. (2010). Evidence for a dynamic spatiotemporal fate map and early fate restrictions of premigratory avian neural crest. Development *137*, 585–595. 10.1242/dev.041509.

11. Furlan, A., and Adameyko, I. (2018). Schwann cell precursor: a neural crest cell in disguise? Developmental Biology *444*, S25–S35. 10.1016/j.ydbio.2018.02.008.

12. Maro, G.S., Vermeren, M., Voiculescu, O., Melton, L., Cohen, J., Charnay, P., and Topilko, P. (2004). Neural crest boundary cap cells constitute a source of neuronal and glial cells of the PNS. Nat Neurosci *7*, 930–938. 10.1038/nn1299.

13. Kastriti, M.E., Faure, L., Von Ahsen, D., Bouderlique, T.G., Boström, J., Solovieva, T., Jackson, C., Bronner, M., Meijer, D., Hadjab, S., et al. (2022). Schwann cell precursors represent a neural crest-like state with biased multipotency. The EMBO Journal *41*, e108780. 10.15252/embj.2021108780.

14. Kameneva, P., Artemov, A.V., Kastriti, M.E., Faure, L., Olsen, T.K., Otte, J., Erickson, A., Semsch, B., Andersson, E.R., Ratz, M., et al. (2021). Single-cell transcriptomics of human embryos identifies multiple sympathoblast lineages with potential implications for neuroblastoma origin. Nat Genet *53*, 694–706. 10.1038/s41588-021-00818-x.

15. Durante, M.A., Rodriguez, D.A., Kurtenbach, S., Kuznetsov, J.N., Sanchez, M.I., Decatur, C.L., Snyder, H., Feun, L.G., Livingstone, A.S., and Harbour, J.W. (2020). Single-cell analysis reveals new evolutionary complexity in uveal melanoma. Nat Commun *11*, 496. 10.1038/s41467-019-14256-1.

16. Grzywa, T.M., Paskal, W., and Włodarski, P.K. (2017). Intratumor and Intertumor Heterogeneity in Melanoma. Transl Oncol *10*, 956–975. 10.1016/j.tranon.2017.09.007.

17. Monroe, C.L., Dahiya, S., and Gutmann, D.H. (2017). Dissecting Clinical Heterogeneity in Neurofibromatosis Type 1. Annu Rev Pathol *12*, 53–74. 10.1146/annurev-pathol-052016-100228.

18. Dong, R., Yang, R., Zhan, Y., Lai, H.-D., Ye, C.-J., Yao, X.-Y., Luo, W.-Q., Cheng, X.-M., Miao, J.-J., Wang, J.-F., et al. (2020). Single-Cell Characterization of Malignant Phenotypes and Developmental Trajectories of Adrenal Neuroblastoma. Cancer Cell *38*, 716-733.e6. 10.1016/j.ccell.2020.08.014.

19. Matthay, K.K., Maris, J.M., Schleiermacher, G., Nakagawara, A., Mackall, C.L., Diller, L., and Weiss, W.A. (2016). Neuroblastoma. Nat Rev Dis Primers *2*, 16078. 10.1038/nrdp.2016.78.

20. Boeva, V., Louis-Brennetot, C., Peltier, A., Durand, S., Pierre-Eugène, C., Raynal, V., Etchevers, H.C., Thomas, S., Lermine, A., Daudigeos-Dubus, E., et al. (2017). Heterogeneity of neuroblastoma cell identity defined by transcriptional circuitries. Nat Genet *49*, 1408–1413. 10.1038/ng.3921.

21. Furlan, A., Dyachuk, V., Kastriti, M.E., Calvo-Enrique, L., Abdo, H., Hadjab, S., Chontorotzea, T., Akkuratova, N., Usoskin, D., Kamenev, D., et al. (2017). Multipotent Peripheral Glial Cells Generate Neuroendocrine Cells of the Adrenal Medulla. Science *357*, eaal3753. 10.1126/science.aal3753.

22. Kastriti, M.E., Kameneva, P., Kamenev, D., Dyachuk, V., Furlan, A., Hampl, M., Memic, F., Marklund, U., Lallemend, F., Hadjab, S., et al. (2019). Schwann Cell Precursors Generate the Majority of Chromaffin Cells in Zuckerkandl Organ and Some Sympathetic Neurons in Paraganglia. Front Mol Neurosci *12*, 6. 10.3389/fnmol.2019.00006.

23. Zeineldin, M., Patel, A.G., and Dyer, M.A. (2022). Neuroblastoma: When differentiation goes awry. Neuron *110*, 2916–2928. 10.1016/j.neuron.2022.07.012.

24. Hwang, W.L., Wolfson, R.L., Niemierko, A., Marcus, K.J., DuBois, S.G., and Haas-Kogan, D. (2018). Clinical Impact of Tumor Mutational Burden in Neuroblastoma. J Natl Cancer Inst *111*, 695–699. 10.1093/jnci/djy157.

25. Subbaraman, N. (2021). Limit on lab-grown human embryos dropped by stem-cell body. Nature *594*, 18–19. 10.1038/d41586-021-01423-y.

26. Rayon, T., Stamataki, D., Perez-Carrasco, R., Garcia-Perez, L., Barrington, C., Melchionda, M., Exelby, K., Lazaro, J., Tybulewicz, V.L.J., Fisher, E.M.C., et al. (2020). Species-specific pace of development is associated with differences in protein stability. Science *369*, eaba7667. 10.1126/science.aba7667.

27. Braekeveldt, N., and Bexell, D. (2018). Patient-derived xenografts as preclinical neuroblastoma models. Cell Tissue Res *372*, 233–243. 10.1007/s00441-017-2687-8.

28. Nolan, J.C., Frawley, T., Tighe, J., Soh, H., Curtin, C., and Piskareva, O. (2020). Preclinical models for neuroblastoma: Advances and challenges. Cancer Letters *474*, 53–62. 10.1016/j.canlet.2020.01.015.

29. Bedoya-Reina, O.C., Li, W., Arceo, M., Plescher, M., Bullova, P., Pui, H., Kaucka, M., Kharchenko, P., Martinsson, T., Holmberg, J., et al. (2021). Single-nuclei transcriptomes from human adrenal gland reveal distinct cellular identities of low and high-risk neuroblastoma tumors. Nat Commun *12*, 5309. 10.1038/s41467-021-24870-7.

30. Rasmuson, A., Segerström, L., Nethander, M., Finnman, J., Elfman, L.H.M., Javanmardi, N., Nilsson, S., Johnsen, J.I., Martinsson, T., and Kogner, P. (2012). Tumor development, growth characteristics and spectrum of genetic

aberrations in the TH-MYCN mouse model of neuroblastoma. PLoS One *7*, e51297. 10.1371/journal.pone.0051297.

31. Veenvliet, J.V., Lenne, P.-F., Turner, D.A., Nachman, I., and Trivedi, V. (2021). Sculpting with stem cells: how models of embryo development take shape. Development *148*, dev192914. 10.1242/dev.192914.

32. Libby, A.R.G., Joy, D.A., Elder, N.H., Bulger, E.A., Krakora, M.Z., Gaylord, E.A., Mendoza-Camacho, F., Butts, J.C., and McDevitt, T.C. (2021). Axial elongation of caudalized human organoids mimics aspects of neural tube development. Development *148*, dev198275. 10.1242/dev.198275.

33. Moris, N., Anlas, K., Schröder, J., Ghimire, S., Balayo, T., Van den Brink, S., Alemany, A., Oudenaarden, A., and Arias, A. (2020). Generating Human Gastruloids from Human Embryonic Stem Cells. Protocol Exchange. 10.21203/rs.3.pex-812/v1.

34. van den Brink, S.C., Alemany, A., van Batenburg, V., Moris, N., Blotenburg, M., Vivié, J., Baillie-Johnson, P., Nichols, J., Sonnen, K.F., Martinez Arias, A., et al. (2020). Single-cell and spatial transcriptomics reveal somitogenesis in gastruloids. Nature *582*, 405–409. 10.1038/s41586-020-2024-3.

35. Olmsted, Z.T., and Paluh, J.L. (2021). Co-development of central and peripheral neurons with trunk mesendoderm in human elongating multi-lineage organized gastruloids. Nat Commun *12*, 3020. 10.1038/s41467-021-23294-7.

36. Turner, D.A., Girgin, M., Alonso-Crisostomo, L., Trivedi, V., Baillie-Johnson, P., Glodowski, C.R., Hayward, P.C., Collignon, J., Gustavsen, C., Serup, P., et al. (2017). Anteroposterior polarity and elongation in the absence of extra-embryonic tissues and of spatially localised signalling in gastruloids: mammalian embryonic organoids. Development *144*, 3894–3906. 10.1242/dev.150391.

37. Anand, G.M., Megale, H.C., Murphy, S.H., Weis, T., Lin, Z., He, Y., Wang, X., Liu, J., and Ramanathan, S. (2023). Controlling organoid symmetry breaking uncovers an excitable system underlying human axial elongation. Cell *186*, 497-512.e23. 10.1016/j.cell.2022.12.043.

38. He, Z., Maynard, A., Jain, A., Gerber, T., Petri, R., Lin, H.-C., Santel, M., Ly, K., Dupré, J.-S., Sidow, L., et al. (2022). Lineage recording in human cerebral organoids. Nat Methods *19*, 90–99. 10.1038/s41592-021-01344-8.

39. Serra, D., Mayr, U., Boni, A., Lukonin, I., Rempfler, M., Challet Meylan, L., Stadler, M.B., Strnad, P., Papasaikas, P., Vischi, D., et al. (2019). Self-

organization and symmetry breaking in intestinal organoid development. Nature *569*, 66–72. 10.1038/s41586-019-1146-y.

40. Beydag-Tasöz, B.S., D'Costa, J.V., Hersemann, L., Lee, B.H., Luppino, F., Kim, Y.H., Zechner, C., and Grapin-Botton, A. (2023). Integrating single-cell imaging and RNA sequencing datasets links differentiation and morphogenetic dynamics of human pancreatic endocrine progenitors. Developmental Cell. 10.1016/j.devcel.2023.07.019.

41. Yanagida, A., Spindlow, D., Nichols, J., Dattani, A., Smith, A., and Guo, G. (2021). Naive stem cell blastocyst model captures human embryo lineage segregation. Cell Stem Cell *28*, 1016-1022.e4. 10.1016/j.stem.2021.04.031.

42. Moris, N., Anlas, K., van den Brink, S.C., Alemany, A., Schröder, J., Ghimire, S., Balayo, T., van Oudenaarden, A., and Martinez Arias, A. (2020). An in vitro model of early anteroposterior organization during human development. Nature *582*, 410–415. 10.1038/s41586-020-2383-9.

43. Sanaki-Matsumiya, M., Matsuda, M., Gritti, N., Nakaki, F., Sharpe, J., Trivedi, V., and Ebisuya, M. (2022). Periodic formation of epithelial somites from human pluripotent stem cells. Nat Commun *13*, 2325. 10.1038/s41467-022-29967-1.

44. Yuan, G., Wang, J., Liu, Z., Chen, M., Zhu, P., Zhang, H., Hu, Z., Cui, Y., Yuan, Y., and Sha, J. (2023). Establishment of a novel non-integrated human pluripotent stem cell-based gastruloid model. Preprint at bioRxiv, 10.1101/2023.06.28.546720 10.1101/2023.06.28.546720.

45. Beccari, L., Moris, N., Girgin, M., Turner, D.A., Baillie-Johnson, P., Cossy, A.-C., Lutolf, M.P., Duboule, D., and Arias, A.M. (2018). Multi-axial self-organization properties of mouse embryonic stem cells into gastruloids. Nature *562*, 272–276. 10.1038/s41586-018-0578-0.

46. Suppinger, S., Zinner, M., Aizarani, N., Lukonin, I., Ortiz, R., Azzi, C., Stadler, M.B., Vianello, S., Palla, G., Kohler, H., et al. (2023). Multimodal characterization of murine gastruloid development. Cell Stem Cell *30*, 867-884.e11. 10.1016/j.stem.2023.04.018.

47. Corallo, D., Frabetti, S., Candini, O., Gregianin, E., Dominici, M., Fischer, H., and Aveic, S. (2020). Emerging Neuroblastoma 3D In Vitro Models for Pre-Clinical Assessments. Frontiers in Immunology *11*.

48. Simunovic, M., and Brivanlou, A.H. (2017). Embryoids, organoids and gastruloids: new approaches to understanding embryogenesis. Development *144*, 976–985. 10.1242/dev.143529.

49. Zhao, Z., Chen, X., Dowbaj, A.M., Sljukic, A., Bratlie, K., Lin, L., Fong, E.L.S., Balachander, G.M., Chen, Z., Soragni, A., et al. (2022). Organoids. Nat Rev Methods Primers *2*, 1–21. 10.1038/s43586-022-00174-y.

50. Cermola, F., D'Aniello, C., Tatè, R., De Cesare, D., Martinez-Arias, A., Minchiotti, G., and Patriarca, E.J. (2021). Gastruloid Development Competence Discriminates Different States of Pluripotency. Stem Cell Reports *16*, 354–369. 10.1016/j.stemcr.2020.12.013.

51. Veenvliet, J.V., Bolondi, A., Kretzmer, H., Haut, L., Scholze-Wittler, M., Schifferl, D., Koch, F., Guignard, L., Kumar, A.S., Pustet, M., et al. (2020). Mouse embryonic stem cells self-organize into trunk-like structures with neural tube and somites. Science *370*, eaba4937. 10.1126/science.aba4937.

52. Ortmann, D., and Vallier, L. (2017). Variability of human pluripotent stem cell lines. Current Opinion in Genetics & Development *46*, 179–185. 10.1016/j.gde.2017.07.004.

53. Rockel, A.F., Wagner, N., Spenger, P., Ergün, S., and Wörsdörfer, P. (2023). Neuro-mesodermal assembloids recapitulate aspects of peripheral nervous system development in vitro. Stem Cell Reports *18*, 1155–1165. 10.1016/j.stemcr.2023.03.012.

54. Stevanovic, M., Drakulic, D., Lazic, A., Ninkovic, D.S., Schwirtlich, M., and Mojsin, M. (2021). SOX Transcription Factors as Important Regulators of Neuronal and Glial Differentiation During Nervous System Development and Adult Neurogenesis. Front Mol Neurosci *14*, 654031. 10.3389/fnmol.2021.654031.

55. Garriock, R.J., Chalamalasetty, R.B., Kennedy, M.W., Canizales, L.C., Lewandoski, M., and Yamaguchi, T.P. (2015). Lineage tracing of neuromesodermal progenitors reveals novel Wnt-dependent roles in trunk progenitor cell maintenance and differentiation. Development *142*, 1628–1638. 10.1242/dev.111922.

56. Martin, B.L., and Kimelman, D. (2012). Canonical Wnt Signaling Dynamically Controls Multiple Stem Cell Fate Decisions during Vertebrate Body Formation. Developmental Cell *22*, 223–232. 10.1016/j.devcel.2011.11.001.

57. Lee, S., Choi, K., Ahn, H., Song, K., Choe, J., and Lee, I. (2005). TuJ1 (class III beta-tubulin) expression suggests dynamic redistribution of follicular dendritic cells in lymphoid tissue. Eur J Cell Biol *84*, 453–459. 10.1016/j.ejcb.2004.11.001.

58. Liu, L., Oura, S., Markham, Z., Hamilton, J.N., Skory, R.M., Li, L., Sakurai, M., Wang, L., Pinzon-Arteaga, C.A., Plachta, N., et al. (2023). Modeling post-implantation stages of human development into early organogenesis with stem-cell-derived peri-gastruloids. Cell, S0092867423007948. 10.1016/j.cell.2023.07.018.

59. Tomellini, E., Lagadec, C., Polakowska, R., and Le Bourhis, X. (2014). Role of p75 neurotrophin receptor in stem cell biology: more than just a marker. Cell. Mol. Life Sci. *71*, 2467–2481. 10.1007/s00018-014-1564-9.

60. Moretti, A., Caron, L., Nakano, A., Lam, J.T., Bernshausen, A., Chen, Y., Qyang, Y., Bu, L., Sasaki, M., Martin-Puig, S., et al. (2006). Multipotent embryonic isl1+ progenitor cells lead to cardiac, smooth muscle, and endothelial cell diversification. Cell *127*, 1151–1165. 10.1016/j.cell.2006.10.029.

61. Boesmans, W., Nash, A., Tasnády, K.R., Yang, W., Stamp, L.A., and Hao, M.M. (2022). Development, Diversity, and Neurogenic Capacity of Enteric Glia. Front Cell Dev Biol *9*, 775102. 10.3389/fcell.2021.775102.

62. Tomolonis, J.A., Agarwal, S., and Shohet, J.M. (2018). Neuroblastoma pathogenesis: deregulation of embryonic neural crest development. Cell Tissue Res *372*, 245–262. 10.1007/s00441-017-2747-0.

63. Ghimire, S., Mantziou, V., Moris, N., and Martinez Arias, A. (2021). Human gastrulation: The embryo and its models. Developmental Biology *474*, 100–108. 10.1016/j.ydbio.2021.01.006.

64. Woodworth, M.B., Girskis, K.M., and Walsh, C.A. (2017). Building a lineage from single cells: genetic techniques for cell lineage tracking. Nat Rev Genet *18*, 230–244. 10.1038/nrg.2016.159.

65. Pablo H., S.-M., and Marianne E., B. (2012). Epithelial to mesenchymal transition: new and old insights from the classical neural crest model. Semin Cancer Biol *22*, 411–416. 10.1016/j.semcancer.2012.04.008.

66. Hovland, A.S., Bhattacharya, D., Azambuja, A.P., Pramio, D., Copeland, J., Rothstein, M., and Simoes-Costa, M. (2022). Pluripotency factors are repurposed to shape the epigenomic landscape of neural crest cells. Developmental Cell *57*, 2257-2272.e5. 10.1016/j.devcel.2022.09.006.

67. M, O., Cs, H., X, H., Rj, D., and Jp, S.-J. (2006). Functional analysis of Sox8 during neural crest development in Xenopus. Development (Cambridge, England) *133*. 10.1242/dev.02558.

68. Huber, K. (2006). The sympathoadrenal cell lineage: specification, diversification, and new perspectives. Dev Biol *298*, 335–343. 10.1016/j.ydbio.2006.07.010.

69. Huber, K., Kalcheim, C., and Unsicker, K. (2009). The development of the chromaffin cell lineage from the neural crest. Auton Neurosci *151*, 10–16. 10.1016/j.autneu.2009.07.020.

70. O'Rahilly, R. (1983). The timing and sequence of events in the development of the human endocrine system during the embryonic period proper. Anat Embryol *166*, 439–451. 10.1007/BF00305929.

71. Tan, W.-H., Gilmore, E.C., and Baris, H.N. (2014). Human Developmental Genetics. In Reference Module in Biomedical Sciences (Elsevier). 10.1016/B978-0-12-801238-3.05488-X.

72. Galdos, F.X., Lee, C., Lee, S., Paige, S., Goodyer, W., Xu, S., Samad, T., Escobar, G.V., Darsha, A., Beck, A., et al. Combined lineage tracing and scRNA-seq reveals unexpected first heart field predominance of human iPSC differentiation. eLife *12*, e80075. 10.7554/eLife.80075.

73. Bao, X., Adil, M.M., Muckom, R., Zimmermann, J.A., Tran, A., Suhy, N., Xu, Y., Sampayo, R.G., Clark, D.S., and Schaffer, D.V. (2019). Gene Editing to Generate Versatile Human Pluripotent Stem Cell Reporter Lines for Analysis of Differentiation and Lineage Tracing. STEM CELLS *37*, 1556–1566. 10.1002/stem.3096.

74. Spanjaard, B., Hu, B., Mitic, N., Olivares-Chauvet, P., Janjuha, S., Ninov, N., and Junker, J.P. (2018). Simultaneous lineage tracing and cell-type identification using CRISPR–Cas9-induced genetic scars. Nat Biotechnol *36*, 469–473. 10.1038/nbt.4124.

75. Kanton, S., Boyle, M.J., He, Z., Santel, M., Weigert, A., Sanchís-Calleja, F., Guijarro, P., Sidow, L., Fleck, J.S., Han, D., et al. (2019). Organoid single-cell genomic atlas uncovers human-specific features of brain development. Nature *574*, 418–422. 10.1038/s41586-019-1654-9.

76. el Azhar, Y., and Sonnen, K.F. (2021). Development in a Dish—In Vitro Models of Mammalian Embryonic Development. Frontiers in Cell and Developmental Biology *9*.

77. van den Brink, S.C., and van Oudenaarden, A. (2021). 3D gastruloids: a novel frontier in stem cell-based in vitro modeling of mammalian gastrulation. Trends in Cell Biology *31*, 747–759. 10.1016/j.tcb.2021.06.007.

78. Zhou, J.-Q., Zeng, L.-H., Li, C.-T., He, D.-H., Zhao, H.-D., Xu, Y.-N., Jin, Z.-T., and Gao, C. (2023). Brain organoids are new tool for drug screening of neurological diseases. Neural Regen Res *18*, 1884–1889. 10.4103/1673-5374.367983.

79. Oginuma, M., Moncuquet, P., Xiong, F., Karoly, E., Chal, J., Guevorkian, K., and Pourquié, O. (2017). A Gradient of Glycolytic Activity Coordinates FGF and Wnt Signaling during Elongation of the Body Axis in Amniote Embryos. Developmental Cell *40*, 342-353.e10. 10.1016/j.devcel.2017.02.001.

80. Takemoto, T., Uchikawa, M., Yoshida, M., Bell, D.M., Lovell-Badge, R., Papaioannou, V.E., and Kondoh, H. (2011). Tbx6-dependent Sox2 regulation determines neural vs mesodermal fate in axial stem cells. Nature *470*, 394–398. 10.1038/nature09729.

81. Ludwig, T.E., Bergendahl, V., Levenstein, M.E., Yu, J., Probasco, M.D., and Thomson, J.A. (2006). Feeder-independent culture of human embryonic stem cells. Nat Methods *3*, 637–646. 10.1038/nmeth902.

82. Gupta, A., Lutolf, M.P., Hughes, A.J., and Sonnen, K.F. (2021). Bioengineering in vitro models of embryonic development. Stem Cell Reports *16*, 1104–1116. 10.1016/j.stemcr.2021.04.005.

83. Leung, A.W., Murdoch, B., Salem, A.F., Prasad, M.S., Gomez, G.A., and García-Castro, M.I. (2016). WNT/β-catenin signaling mediates human neural crest induction via a pre-neural border intermediate. Development *143*, 398–410. 10.1242/dev.130849.

84. Minn, K.T., Fu, Y.C., He, S., Dietmann, S., George, S.C., Anastasio, M.A., Morris, S.A., and Solnica-Krezel, L. (2020). High-resolution transcriptional and morphogenetic profiling of cells from micropatterned human ESC gastruloid cultures. eLife *9*, e59445. 10.7554/eLife.59445.

85. Karzbrun, E., Khankhel, A.H., Megale, H.C., Glasauer, S.M.K., Wyle, Y., Britton, G., Warmflash, A., Kosik, K.S., Siggia, E.D., Shraiman, B.I., et al. (2021). Human neural tube morphogenesis in vitro by geometric constraints. Nature *599*, 268–272. 10.1038/s41586-021-04026-9.

86. Bérenger-Currias, N.M., Mircea, M., Adegeest, E., van den Berg, P.R., Feliksik, M., Hochane, M., Idema, T., Tans, S.J., and Semrau, S. (2022). A gastruloid model of the interaction between embryonic and extra-embryonic cell types. J Tissue Eng *13*, 20417314221103042. 10.1177/20417314221103042.

87. Girgin, M.U., Broguiere, N., Hoehnel, S., Brandenberg, N., Mercier, B., Arias, A.M., and Lutolf, M.P. (2021). Bioengineered embryoids mimic post-

implantation development in vitro. Nat Commun *12*, 5140. 10.1038/s41467-021-25237-8.

88. Cordero, D.R., Brugmann, S., Chu, Y., Bajpai, R., Jame, M., and Helms, J.A. (2011). Cranial neural crest cells on the move: their roles in craniofacial development. Am J Med Genet A *155A*, 270–279. 10.1002/ajmg.a.33702.

89. Le Lièvre, C.S., and Le Douarin, N.M. (1975). Mesenchymal derivatives of the neural crest: analysis of chimaeric quail and chick embryos. J Embryol Exp Morphol *34*, 125–154.

90. Chitrangi, S., Vaity, P., Jamdar, A., and Bhatt, S. (2023). Patient-derived organoids for precision oncology: a platform to facilitate clinical decision making. BMC Cancer *23*, 689. 10.1186/s12885-023-11078-9.

91. Akhtar, A.A., and Breunig, J.J. (2017). Tetracycline-inducible and reversible stable gene expression in human iPSC-derived neural progenitors and in the postnatal mouse brain. Curr Protoc Stem Cell Biol *41*, 5A.9.1-5A.9.12. 10.1002/cpsc.28.

92. Raabe, E.H., Laudenslager, M., Winter, C., Wasserman, N., Cole, K., LaQuaglia, M., Maris, D.J., Mosse, Y.P., and Maris, J.M. (2008). Prevalence and functional consequence of PHOX2B mutations in neuroblastoma. Oncogene *27*, 469–476. 10.1038/sj.onc.1210659.

Abstract (DE)

Die multipotenten Zellen der Neuralleiste und ihre ebenfalls multipotenten Nachkommen Schwann-Zell-Vorläufer differenzieren in eine Vielzahl von unterschiedlichen Zelltypen, darunter beispielsweise Nerven und Glia des peripheren Nervensystems oder Melanozyten. Des Weiteren wurden die beiden Vorläuferpopulationen als Ursprung in Krankheiten wie dem frühkindlichem Tumor Neuroblastom impliziert. Trotz ihrer Wichtigkeit in Entwicklung und Krankheit ist nicht viel über Differenzierung und Übergangs-zell-status der menschlichen Neuralleiste und Schwann-Zell-Vorläufer bekannt. Dem zugrunde liegt vor allem der Mangel an Versuchsmodellen, die über ausreichende Komplexität verfügen, um die menschliche Embryonalentwicklung zu replizieren. In dieser Arbeit adaptieren wir ein bestehendes, auf menschlichen induzierten pluripotenten Stammzellen basierendes Model der Gastrulation. Wir zeigen, dass unser *in vitro* Model embryonale Entwicklungsschritte wie frühe Bildung der Körperachsen repliziert und Zellen positiv für Marker der Neuralleiste, sowie nerv-verbundenen Schwann-Zell-Vorläufer aufweist. Des Weiteren zeigt das hier vorgestellte Modell Expression von Zell-typ-spezifischen Markern für reife, von der Neuralleiste und/oder Schwann-Zell-Vorläufern abspannenden Zell-typen (sensorische-, autonome Neuronen und Chromaffin Zellen). Zuletzt untermauern unsere Ergebnisse die Notwendigkeit für strenge Kontrollen des Pluripotenz-status von induzierten pluripotenten Zellen und implizieren mögliche gerichtete Anpassung von Zellkultur-bedingungen abhängig vom individuellen Pluripotenz-status der Zelllinie. Zusammenfassend: Das hier vorgestellte in-vitro-Modell bietet eine neue Plattform zur Untersuchung der molekularen Determinanten der Differenzierung von Neuralleiste und Schwann-Zell-Vorläufern, Charakterisierung von Übergangs-zell-status und bösartigen Veränderungen in hoher räumlich-zeitlicher Auflösung.

Supplementary Figures

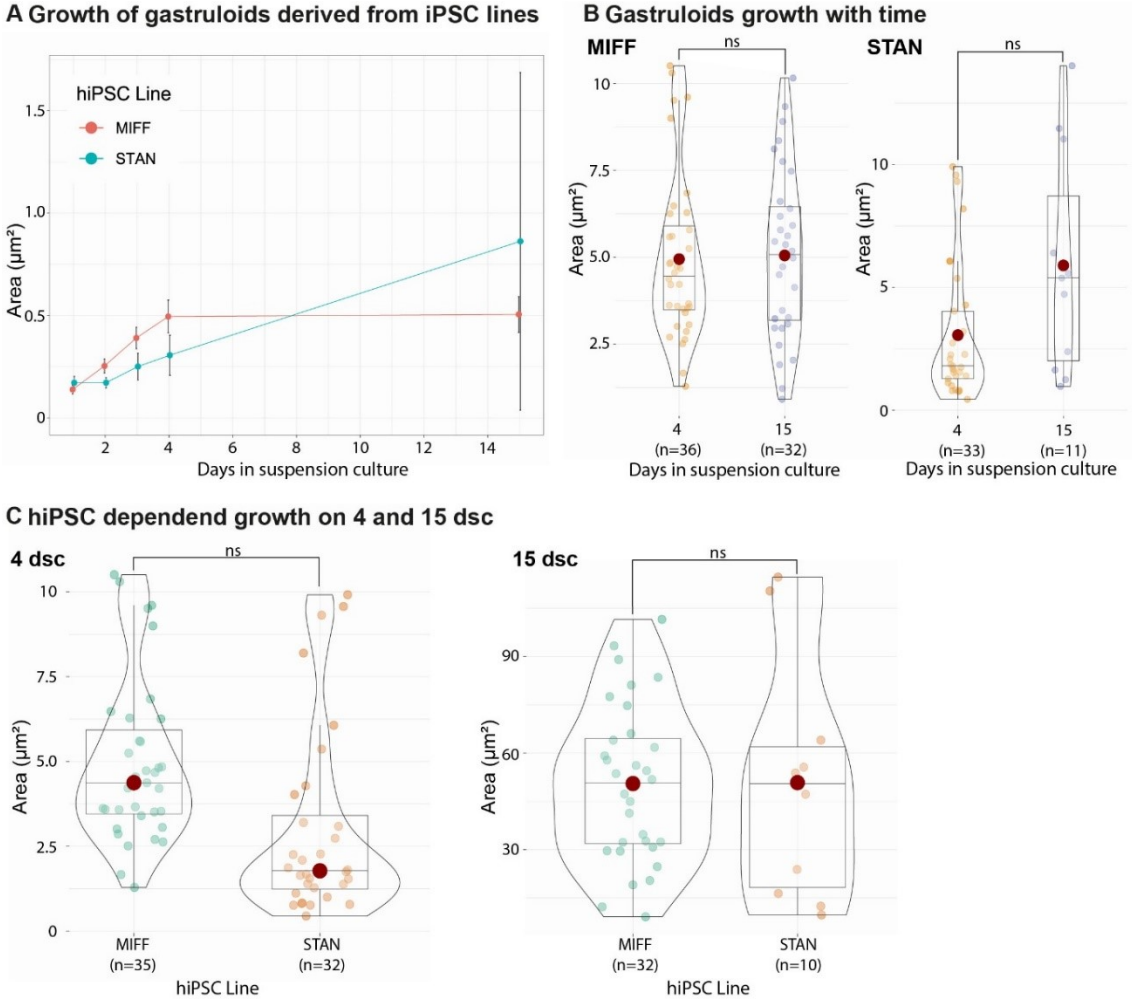

Supplementary Figure 1: The iPSC line used for the establishment of gastruloids does not affect their growth. *A) Linear regression of growth of gastruloids generated from MIFF- (red) and STAN- (blue) iPSC lines measured by area (µm2) on 1-, 2-, 3-, 4- and 15 dsc. Y-axis values labeled to the power of 105. (B) Violin plot showing MIFF- and STAN-derived gastruloids area (µm2) on 4- and 15 dsc using Student t-test, p-value - * < 0.05, ** < 0.01,***<0.001, ns > 0.05. n is the number of quantified gastruloids per group. Y-axis values labeled to the power of 104. (C) Violin plot comparing MIFF- (green) and STAN- (orange) derived gastruloids area (µm2) after 4- and 15 dsc by Student t-test, p-value - * < 0.05, ** < 0.01,***<0.001, ns > 0.05. n is the number of quantified gastruloids per group. Y-axis values labeled to the power of 104 and 103.*

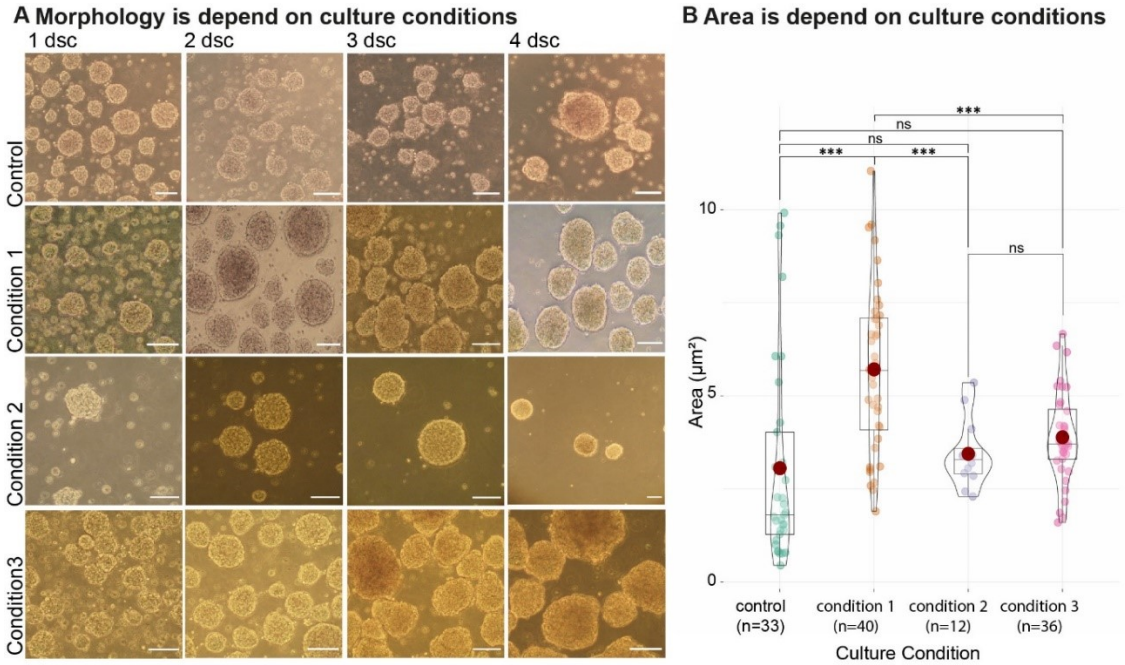

Supplementary Figure 2: Effects of culture conditions on gastruloid morphology. *Comparing: control (E8, 1x GF), condition 1 (mTESRplus, 3xGF), condition 2 (mTESRplus, 1xGF), and condition 3 (E8, 3xGF). (A) Phase contrast images of iPSC line STAN, cultured in N2B27 for 4 dsc comparing condition 1, condition 2, and condition 3. Scale bars: 100 µm. (B) Violin plot comparing gastruloids area (µm2) after 4 dsc by ANOVA comparing control (green), condition 1 (orange), condition 2 (violet), and condition 3 (red). P value - * < 0.05, ** < 0.01,***<0.001, ns > 0.05. n is the number of quantified gastruloids per group. Y-axis values labeled to the power of 104.*

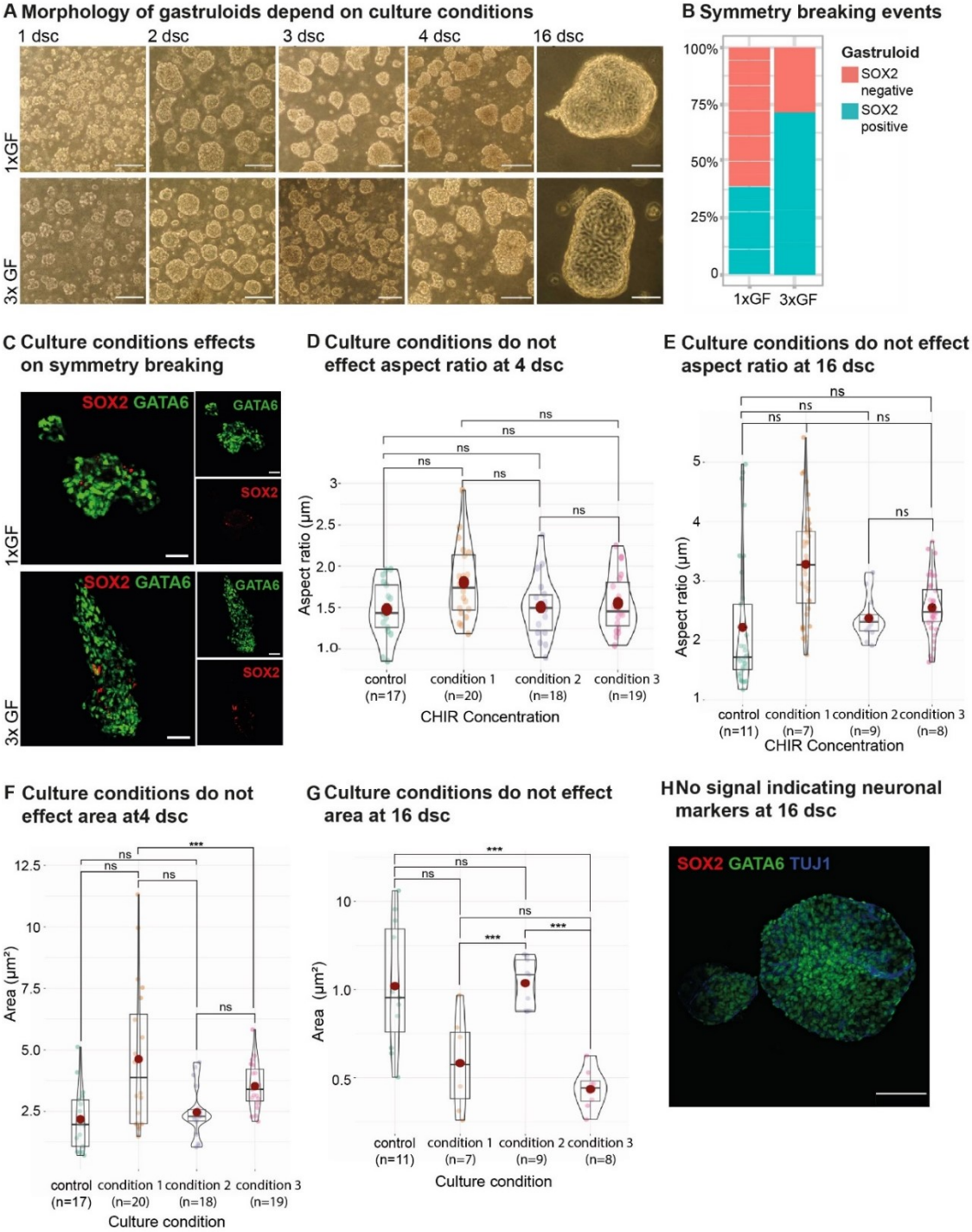

Supplementary Figure 3: Combinatory effects of culture conditions on early gene expression and morphological characteristics of STAN-derived gastruloids. *(A) Phase contrast images of iPSC line STAN, cultured in N2B27 for 16 dsc comparing 1xGF and 3xGF concentrations. Scale bars: 100 µm. (B) Percentage of gastruloids with SOX2-positive cells on 4 dsc comparing 1xGF and 3xGF conditions. (C) Immunofluorescence images of gastruloids derived from STAN iPSC after 4 dsc showing SOX2 (red) and GATA6 (green). Gastruloids were subjected to either 1xGF or 3xGF conditions during shaking culture. Scale bars: 20 µm. D-F: Effects of culture conditions on gastruloid morphology comparing control (3.0µM CHIR, 1xGF), condition 1 (3.3µM CHIR, 1xGF), condition 2 (3.0µM CHIR, 3xGF), and condition 3 (3.3µM CHIR, 3xGF). (D) Violin plot comparing STAN-derived gastruloids aspect ratio after 4 dsc showing no significant effects of culture conditions on elongation of gastruloids. Comparison of aspect ratios was done using Welch-ANOVA, p-value - * < 0.05, ** < 0.01,***<0.001, ns > 0.05. n is the number of quantified gastruloids per group. (E) Violin plot comparing STAN-derived gastruloids aspect ratio on 16 dsc showing*

*no significant effects of culture conditions on elongation of gastruloids. Comparison of aspect ratios was done using Welch-ANOVA, p-value - * < 0.05, ** < 0.01,***<0.001, ns > 0.05. n is the number of quantified gastruloids per group. (F) Violin plot comparing STAN-derived gastruloids on 4 dsc showing significant effects of culture conditions on gastruloid size only between control and condition 3. Comparison of area measurements was done using Welch-ANOVA p value - * < 0.05, ** < 0.01,***<0.001, ns > 0.05. n is the number of quantified gastruloids per group. (G) Violin plot comparing STAN-derived gastruloids area after 16 dsc showing significantly higher gastruloid size in culture conditions using initial CHIR concentrations. Comparison of area measurements was done using Welch-ANOVA p value - * < 0.05, ** < 0.01,***<0.001, ns > 0.05. n is the number of quantified gastruloids per group. (H) Immunofluorescence image of gastruloids derived from STAN iPSC on 16 dsc, showing SOX2 (red) and GATA6 (green) and TUJ1 (blue). Gastruloid starting material was cultured in either (mTESRplus media and submitted to 3xGF and 3.6µm CHIR. Scale bar: 100 µm.*

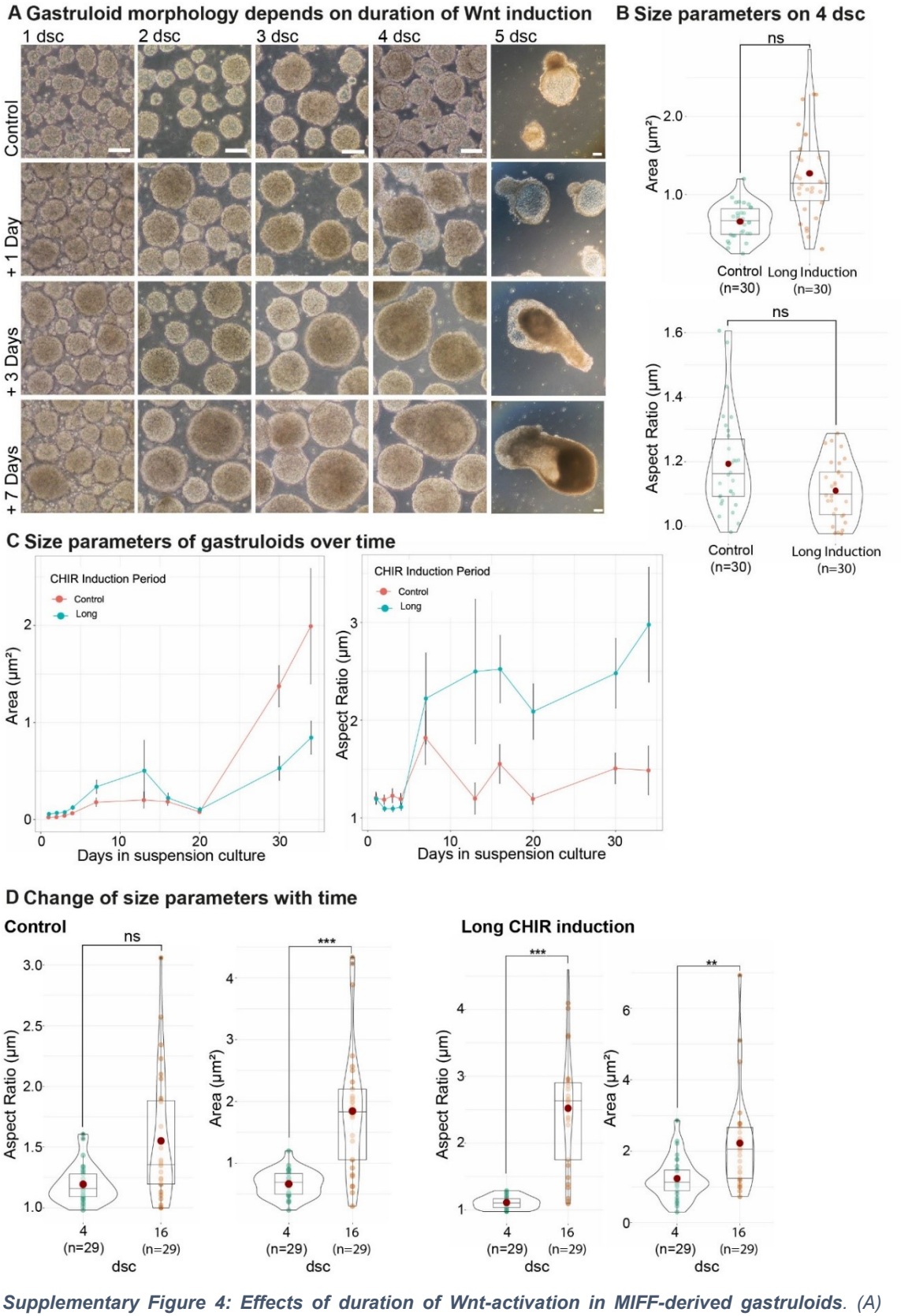

Supplementary Figure 4: Effects of duration of Wnt-activation in MIFF-derived gastruloids. *(A) Phase contrast image of MIFF-derived gastruloids cultured in N2B27 for 1-,2-,3-,4- and 5 dsc. iPSC were induced for 2 days (control) in 2D culture, or 2 days in 2D culture, and 7 additional dsc (+7 days). Scale bars: 100 µm. (B) Violin plot showing MIFF-derived gastruloids aspect ratio and area on 4 dsc, comparing effects of control (green) and long (orange) CHIR induction. Statistical analysis was performed using Students' t-tests p value - * < 0.05, ** < 0.01,***<0.001, ns > 0.05. n is the number of quantified gastruloids per group. Y-axis of area measurements to the power of 106. (C) Linear regression of gastruloid size and*

*elongation measurements of MIFF-derived gastruloids submitted to control (red) and long (blue) CHIR induction. Measurements were performed on 1-, 2-, 3-, 4-, 7-, 14-, 16-, 20-, 30- and 34 dsc. Y-axis of area measurements to the power of 106. (D) Violin plot comparing gastruloid size parameters area and aspect ratio between 4 dsc (green) and 16 dsc (orange) in gastruloids submitted to control and long CHIR induction. Statistical analysis was performed using Students' t-test, p-value - * < 0.05, ** < 0.01,***<0.001, ns > 0.05. Y-axis of area measurements to the power of 10^5.*

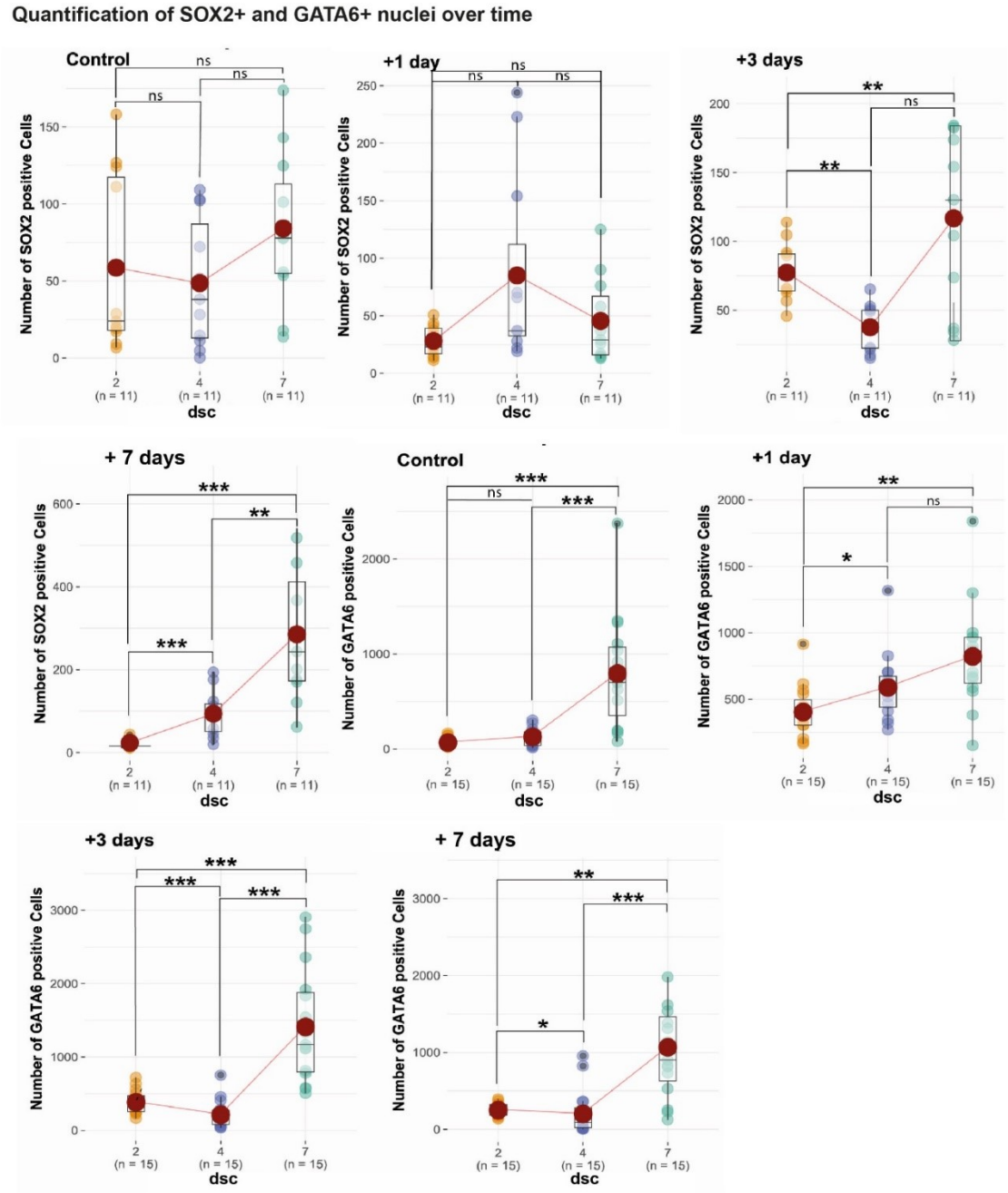

Supplementary Figure 5: Effects of duration of WNT-activation in MIFF-derived gastruloids SOX2 and GATA6 expression. *Box plot showing MIFF-derived gastruloids number of SOX2+ or GATA6+nuclei per treatment group on 2-, 4- and 7 dsc. Statistical analysis was done using Welch-ANOVA, p-value - * < 0.05, ** < 0.01,***<0.001, ns > 0.05.. n is the number of quantified gastruloids per group.*

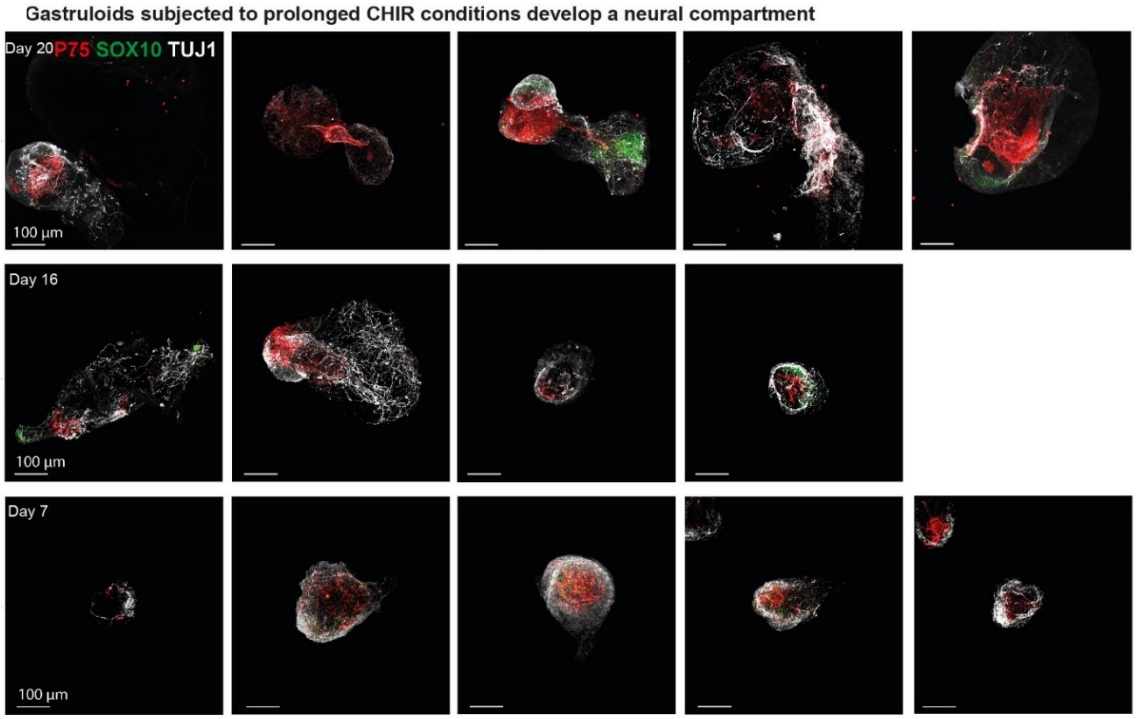

Supplementary Figure 6: Presence of neural compartment in MIFF-derived gastruloids subjected to prolonged CHIR exposure. *Maximum intensity projections of immunofluorescent whole mount of TUJ1 (white) and P75 (red) sorted according to the time point of sample collection. Scale bar: 100um.*

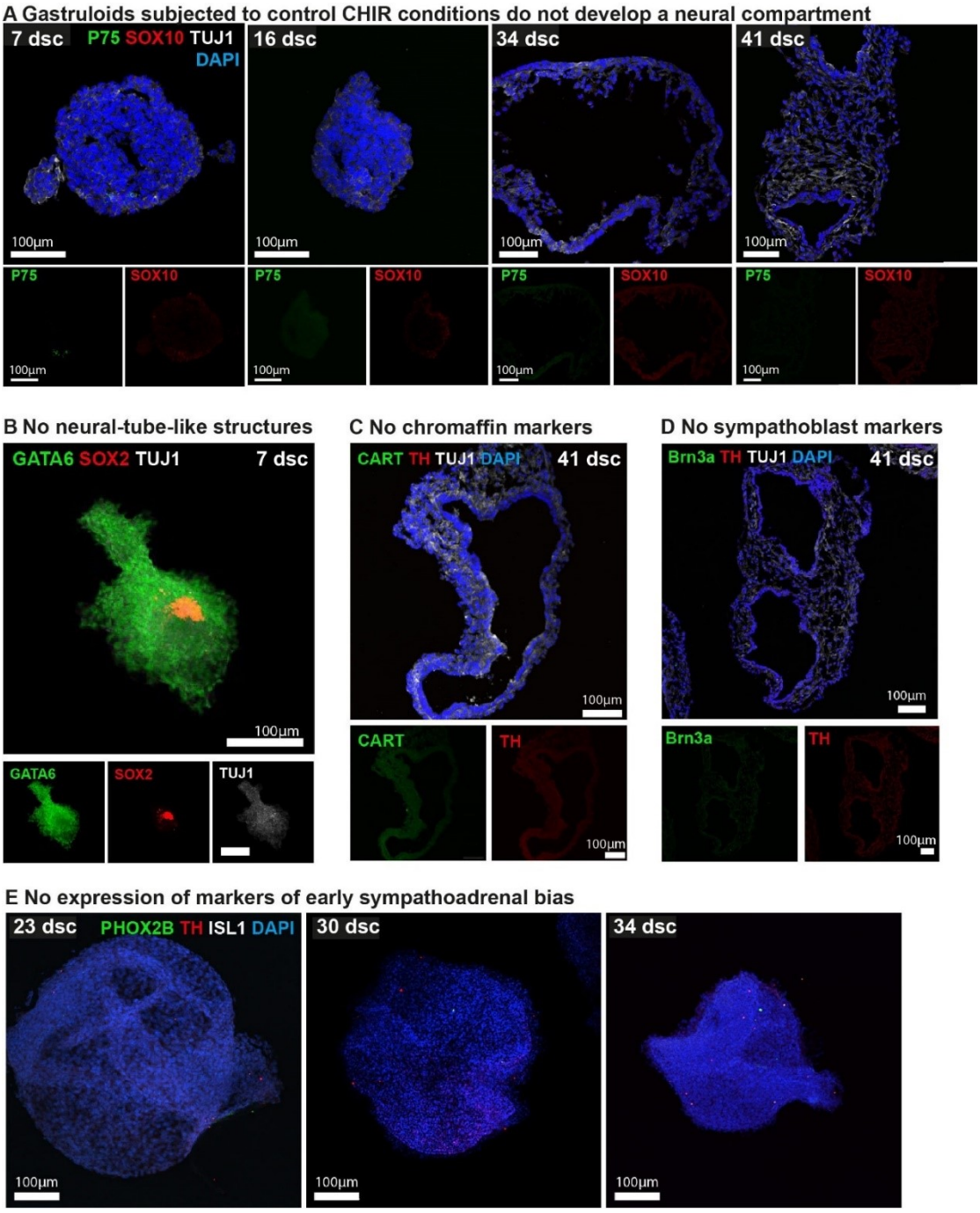

Supplementary Figure 7: Gastruloids subjected to control CHIR induction period do not show NCC and nerve-associated SCPs. *(A) Immunofluorescent image of P75 (green), SOX10 (red), and TUJ1 (white) of sections of gastruloids subjected to control conditions. (B) Maximum intensity projection of immunofluorescent whole mount of GATA6 (green), SOX2 (red), and TUJ1 (white) of 7 dsc gastruloids showing no clear nervous compartment or SOX2+ tube-like structures. (C) Immunohistochemistry of sections for chromaffin markers CART (green), TH (red), and TUJ1 (white) on sections of 41 dsc gastruloids. (D) Immunohistochemistry for sensory neuron markers BRN3A (green), TH (red), and TUJ1 (white) on sections of gastruloids after 41 dsc. (F) Maximum intensity projections of the immunofluorescent whole mount of PHOX2B (green), TH (red), and ISL1/2 (white) sorted according to the time point of sample collection.*

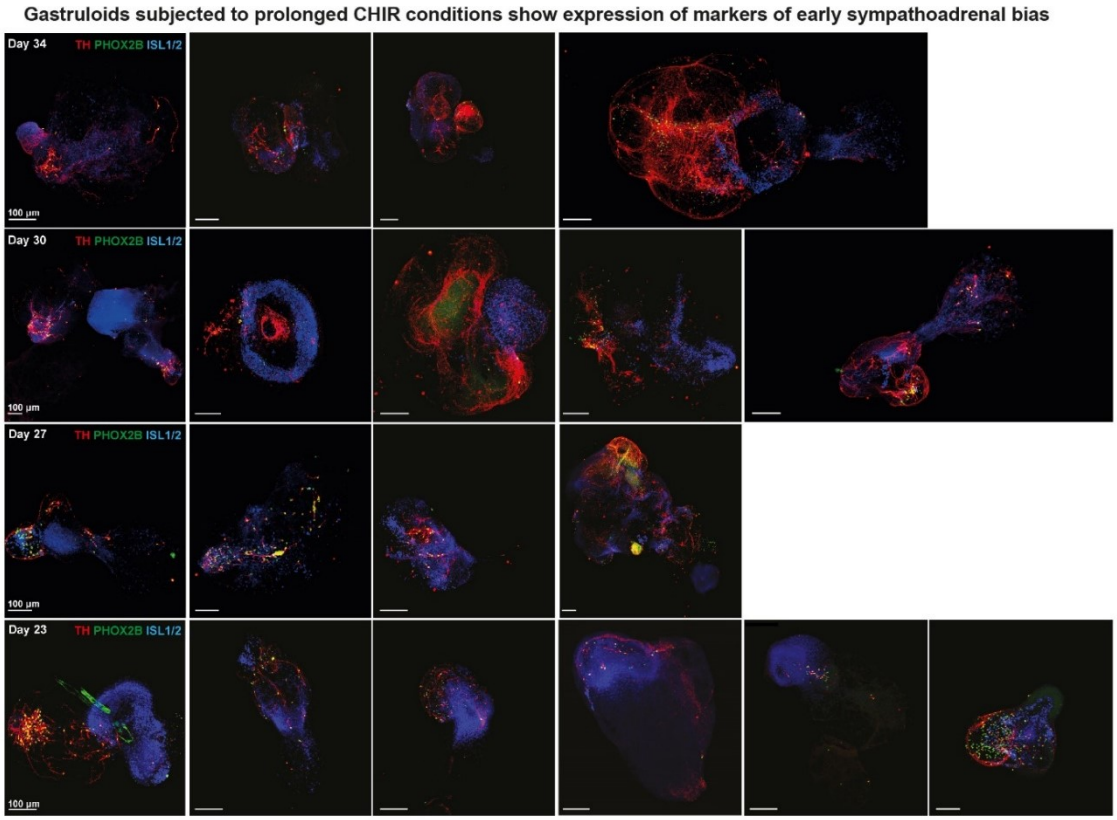

Supplementary Figure 8: Presence of potential sympathoadrenal progenitors in MIFF-derived gastruloids subjected to prolonged CHIR exposure*. Maximum intensity projections of the immunofluorescent whole mount of PHOX2B (green), TH (red), and ISL1/2 (blue) sorted according to the time point of sample collection. Scale bar 100um.*

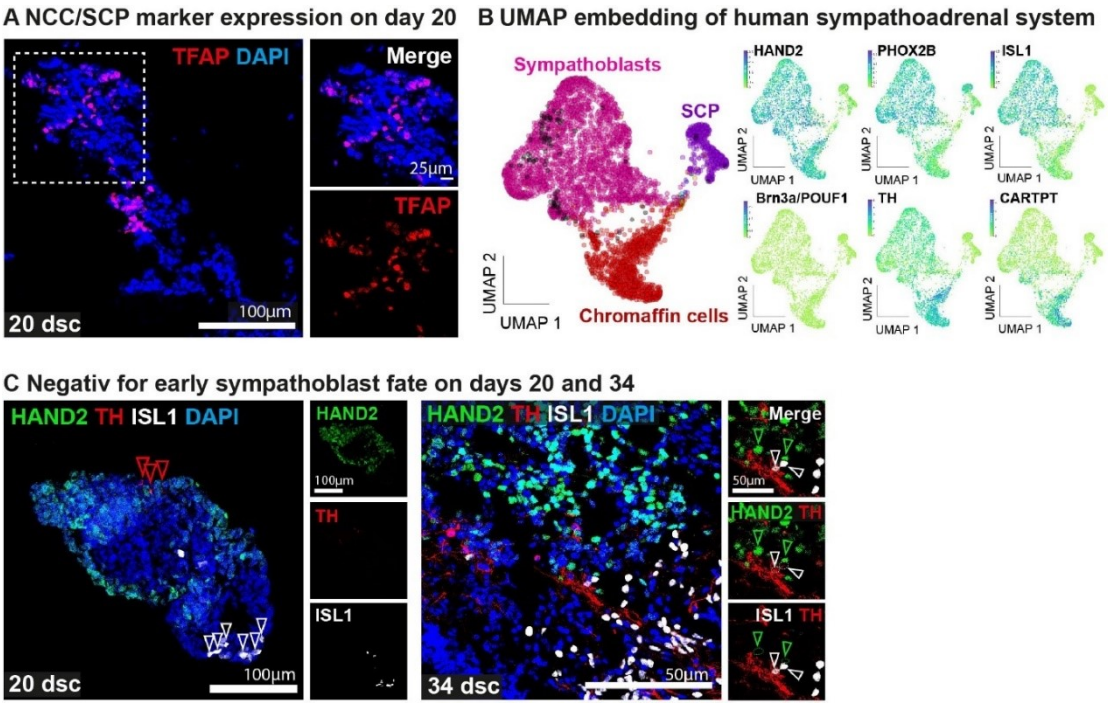

Supplementary Figure 9: Presence of NCCs/SCPs lineage-derived cell types within MIFF-derived gastruloids subjected to prolonged CHIR induction. *(A) Immunofluorescent image of TFAP+ (red) nuclei in sections of day 20 gastruloids. (B) Marker gene expression of HAND2, PHOX2B, ISL1/2, BRN3A, TH, and CARTPT shown on UMAP embedding of developing human sympathoadrenal system generated by Kameneva et al. (2021). (C) Immunofluorescent image of HAND2 (green), TH (red), and ISL1 (white) of sections of gastruloids after 20 dsc and 34 dsc, showing no HAND2+/TH+/ISL1+ transitory cell states. Green arrowheads and outlines indicate HAND2+/TH-/ISL- nuclei. White arrowheads and outlines indicate ISL1+/HAND2-/TH- nuclei.*